Marine and Petroleum Geology 68 (2015) 806–823

Contents lists available at ScienceDirect

Marine and Petroleum Geology

journal homepage: www.elsevier.com/locate/marpetgeo

Research paper

The fate of bubbles in a large, intense bubble megaplume for stratified and unstratified water: Numerical simulations of 22/4b expedition field data

Ira Leifer[a,*], Evan Solomon[b], Jens Schneider von Deimling[c], Gregor Rehder[d], Rick Coffin[e], Peter Linke[c]

[a] Bubbleology Research International, Solvang, CA 93463, USA
[b] School of Oceanography, University of Washington, Seattle, WA 98195, USA
[c] GEOMAR Helmholtz Centre for Ocean Research Kiel, Germany
[d] Leibniz Institute for Baltic Sea Research, Warnemuende, Germany
[e] Texas A&M University, Corpus Christi, TX 78412, USA

ARTICLE INFO

Article history:
Received 1 January 2014
Received in revised form 24 July 2015
Accepted 27 July 2015

Keywords:
Bubble plume
Numerical model
Atmospheric methane measurements
North sea
Seepage
Blowout
22/4b
Vortical motions
Bubble gas exchange

ABSTRACT

Extremely intense bubble plumes, like the North Sea 22/4b blowout megaplume (defined as more than 10^6 L day^{-1}), create very strong upwelling flows (>1 m s^{-1}), which lead to detrainment of methane-enriched water, but leave direct bubble-mediated transport unaffected. Dissolved CH_4 depth profiles and atmospheric measurements during a fall 2011 survey of the 22/4b site suggest strong constraint of seabed CH_4 below the thermocline. Seabed bubbles were nearly pure CH_4.

The effect of the upwelling flow on the fate of bubble plume CH_4 was investigated with a numerical bubble-propagation model. The model considered different representative bubble plume size distributions, ϕ, and a global (total) megaplume bubble size distribution, Φ, synthesized from video survey data and ϕ from the literature. Simulations showed that none of the literature plumes or variations in the upwelling flow could constrain CH_4 sufficiently below the thermocline.

Two new bubble megaplume processes were simulated, vortical bubble trapping (slow rise) and a hypothesized, enhanced bubble gas exchange, k_{BE}, an enhancement factor applied to the normal bubble gas exchange rate, k_B. The latter could arise from plume turbulence increasing bubble boundary-layer turbulence and thus its gas exchange. Observations could not be reproduced solely by slow rise, however, simulations with k_{BE}~6 reproduced observational constraints, as could weaker k_{BE} in conjunction with slow rise.

Field validation of k_{BE} is needed given its implications for the fate of megaplume CH_4 emissions (anthropogenic or natural) for stratified and unstratified conditions. k_{BE} suggests marine CH_4 geologic contributions to the atmosphere from all but shallow waters primarily arises from bubble plumes that are less than megaplume size.

1. Introduction

In 1990, a gas blowout occurred in the central UK North Sea, ~200 km from the Scottish mainland 57.922°N, 1.6325°E (WGS84 UTM: 418997 east, 6421081 north). Although the initial bubble plume had a massive surface expression (~order 1 km), it dwindled rapidly after a few days (Leifer and Judd, 2015) to a shadow of its former size. Although expected to diminish further rapidly afterwards, it has persisted over the decades to the present (Rehder et al., 1998; Schneider von Deimling et al., 2007; Schneider von Deimling et al., 2015). The plume, (or megaplume) escapes from a slightly asymmetric conical crater, ~50 m in diameter at the rim, descending to a small crater floor ~22 m below the surrounding 100-m deep seabed (Leifer, 2015). The 22/4b blowout seabed flux is the largest published flux to date by an order of magnitude (dis-

* Corresponding author. Bubbleology Research International, Solvang, CA 93463, USA.
E-mail addresses: ira.leifer@bubbleology.com (I. Leifer), esolomn@uw.edu (E. Solomon), plinke@geomar.de (J. Schneider von Deimling), gregor.rehder@io-warnemuende.de (G. Rehder), richard.coffin@tamucc.edu (R. Coffin), plinke@ifm-geomar.de (P. Linke).

http://dx.doi.org/10.1016/j.marpetgeo.2015.07.025
0264-8172/

cussed in Section 1.2), with seabed emissions estimated at 90 L s^{-1} (102 m, 9.5 °C) in an uncertainty range of 50–142 L s^{-1} (Leifer, 2015).

Although the 22/4b megaplume is anthropogenic in origin, megaplume seepage also occurs naturally. For example, a number of megaplume seeps have been quantified in the Coal Oil Point (COP) seep field (Boles et al., 2001; Clark et al., 2010). Megaplumes are defined as releasing more than 10^6 L day^{-1} at the seabed and exhibit distinct characteristics compared to smaller bubble plumes. Although seep megaplumes can arise from a single vent (particularly for an anthropogenic source such as a pipeline leak), they also can arise from numerous seabed seep bubble vents that are located within a spatially constrained and limited area (Leifer, 2015; Leifer et al., 2004, 2010). As these individual plumes rise, they merge into a single bubble plume after rising a short distance, "forgetting" their individual plume characteristics.

Currently, the megaplume seepage contribution to regional and global budgets of the important greenhouse gas, methane, CH_4, largely is unknown because few observations exist. In fact, there is significant uncertainty in the contribution of normal (not megaplume) marine seepage CH_4 to atmospheric greenhouse gas budgets due to few seabed measurements and uncertainty about water-column losses from dissolution – i.e., bubble transport efficiency. Yet, natural global terrestrial and marine emissions could be 45 Tg yr^{-1} (Kvenvolden and Rogers, 2005), with additional marine CH_4 seepage contributions from Arctic submerged permafrost of 18 Tg yr^{-1} (Shakhova et al., 2014).

1.1. Manuscript overview

To understand better the regional CH_4 contribution of a large blowout plume, a campaign was conducted to the 22/4b well site in the north–central North Sea (Fig. 1) on the 62-m survey vessel, *Pathfinder* (Supp. Fig. S1 – supplemental figures provide additional information and are denoted with "S"). The survey sought to measure seabed bubble fluxes and determine the fate of this CH_4 (Leifer and Judd, 2015). A number of observations made during the study, presented in Section 2 and in this special issue (Gerilowski et al., 2015; Judd, 2015; Schneider von Deimling et al., 2015), suggest negligible transport to the upper water column and atmosphere. This is seemingly inconsistent with bubble understanding where large bubbles in a strong upwelling flow should transport significant CH_4 across only 100 m of water column to the atmosphere (Leifer and Patro, 2002) and even from far deeper (Solomon et al., 2009). Herein, we compare water column and atmospheric measurements with numerical bubble model simulations to evaluate the underlying megaplume bubble transport processes controlling the fate of seabed CH_4.

Specifically, we explore two hypotheses that could explain these observations using a numerical bubble propagation model (Leifer and Patro, 2002) that has been field validated (Rehder et al., 2009), including application to marine megaplume observations (Leifer et al., 2006), which makes it unique. In particular, this model incorporates upwelling flows (Leifer et al., 2006) which play a critical role in understanding the phenomena. The other bubble propagation model in the literature (McGinnis et al., 2006) neglects these upwelling flows. Furthermore, continuum bubble plume models, e.g., Socolofsky et al. (2011), do not discriminate between large and small bubbles, even though their fates are highly disparate (Leifer and Patro, 2002), thus such models are a poor tool to investigate the underlying bubble processes in megaplumes.

Below we review bubble processes, bubble plume processes, and megaplume bubble processes including the basic equations of the numerical bubble propagation model. This model is used to predict the fate of bubbles in a blowout megaplume and their transported gas, for comparison with water-column observations. The model is initialized with the observed seabed gas composition and a synthetic global bubble size distribution, Φ, based upon video plume characterization survey data (Leifer, 2015) and literature bubble size distributions (Leifer, 2010). The model also includes the observed upwelling flows, discussed in Nauw et al. (2015b) and Wiggins et al. (2015), which is the most significant factor driving the predicted fate of the plume bubbles. The very strong upwelling flow drives extremely rapid bubble rise such that the model predicts nearly all bubbles reach the sea surface with significant CH_4, in sharp contrast to observations. The simulations are discussed in terms of the underlying processes and the larger implications of the two new hypothesized mechanisms attempting to explain observations proposed mechanisms. Additional figures and information can be found in the supplemental materials.

1.2. Bubbles and bubble plumes

Bubble fate varies strongly and non-linearly with size (Leifer and Patro, 2002) with smaller bubbles dissolving and larger bubbles growing. For shallow seas and near coastal waters at depths between 10 and 100 m, a significant fraction of the seabed bubble CH_4 is transported directly to the atmosphere (Leifer and Patro, 2002), but even for far deeper waters, the atmospheric contribution can be non-negligible, e.g., see Solomon et al. (2009) for 550 m, Gulf of Mexico.

As the bubble rises, bubble evolution is described by a series of coupled differential equations – see Leifer and Patro (2002) and Solomon et al. (2009). The differential equation for bubble size change with time, t, is derived from the ideal gas law and is:

$$\frac{\partial r}{\partial t} = \left\{ \frac{\boldsymbol{R}T}{\zeta}\frac{\partial n}{\partial t} - \frac{4\pi r^3}{3}\rho_w g\frac{\partial z}{\partial t} \right\} \Big/ \left\{ 4\pi r^2 P_B - \frac{4\pi r^3}{3}\frac{2\sigma}{r^2} \right\} \tag{1}$$

where r is the equivalent spherical radius, $\boldsymbol{R}$ is the ideal gas law constant, T is temperature, n is the bubble molar content, ρ_w is the water density, g is gravity, z is depth, P_B is bubble pressure, σ is the surface tension or LaPlace pressure, and ζ is compressibility, which is 1.0 at the sea surface, and non-unity only for typical composition seep bubbles at depths of more than a few hundred meters.

The bubble gas exchange flux, f, is driven by a concentration gradient (incorporating solubility) across the bubble interface with surface area, A, and depends on the individual bubble gas exchange rate, $k_B(r,Sc_i,T)$, where i is the i^{th} gas species. k_B depends on the bubble hydrodynamics, typically parameterized with respect to the stagnant buoyancy rise velocity, $V_B(r,T)$, which in turn depends on the interfacial mobility – or immobility if contaminated. k_B is a piecewise function for contaminated and uncontaminated bubbles from Clift et al. (1978; Eqns. 3–45, 3–52; 5–37), as is $V_B(r,T)$, which is from Leifer et al. (2000b). Most marine seep bubbles are in the range $1000 < r < 3000$ μm (Leifer, 2010; Leifer and Culling, 2010) and behave hydrodynamically clean (Patro et al., 2002), however, as the bubble dissolves, it may get small enough to behave contaminated.

The gas exchange flux, f_i is:

$$\begin{aligned} f_i = \frac{\partial n_i}{\partial t} &= k_B(r, Sc_i, T)4\pi r^2(\Delta C_i) \\ &= k_B(r, Sc_i, T)4\pi r^2\left(C_i - k_\beta(z, i, T)H_i(T)P_i\right) \end{aligned} \tag{2}$$

where n_i is the bubble molar content, C_i is the aqueous concentration, H_i is the Henry's Law constant solubility (mol/cm^3/atm), and $k_\beta(z,i,T)$ is a function of gas species and combines with H_i to describe the pressure (depth) dependency in gas solubility – i.e., $k_\beta(z,i)H_i$, and is 1.00 at the sea surface. Total bubble moles, $n = \Sigma n_i$. The bubble partial pressure, P_{Bi}, decreases as:

$$P_{Bi} = \frac{n_i}{n}(P_A + \rho_w g z + 2\sigma/r) \tag{3}$$

Fig. 1. North Sea map showing location of the 22/4b study site. Color shows water depth. (wikipedia commons, 2015) (For interpretation of the references to color in this figure legend, the reader is referred to the web version of this article.).

where P_A is atmospheric pressure and total bubble pressure, $P_B = \Sigma P_{Bi}$. One important aspect of bubble gas exchange is that large changes of the major gases' molar content (typically CH_4 and air for seep bubbles) drive changes in n, which affects P_{Bi} (Eqn. (3)) and thus the exchange of minor gases (Eqn. (2)) – enhancing outgassing (for major gas outflow, i.e., bubble shrinkage) or uptake (for major gas inflow, i.e., bubble growth) (Leifer and Clark, 2002).

Bubble dissolution (or gas uptake) strongly depends on z via the hydrostatic pressure and concentration difference (Eqn. (2)) and also depends on r (Leifer and Patro, 2002) – large bubbles are far more efficient at vertical gas transport, largely due to their greater volume to surface area ratio and due to their faster V_B. As a result, the entire plume size range needs consideration to account for different bubble fates with size (Leifer and Patro, 2002).

An important plume process arises where plume concentrations become enhanced in bubble gases (or depleted in dissolved gases), decreasing the concentration gradient that drives gas exchange (Eqn. (2)). For highly insoluble gases, this can occur at quite low concentrations and can be important even at significant depths; for others, such as air, it likely is important only near the sea surface.

The final differential equation for the bubble vertical rise, $\partial z/\partial t$ is:

$$\frac{\partial z}{\partial t} = V_B(r) + V_F(Q(z)) \tag{4}$$

where V_F is the sum of vertical fluid motions and most importantly includes the plume upwelling flow, V_{up}, which is the upwards fluid motions driven by the rising bubbles. V_{up} is weakly dependent on the bubble plume volume flux, Q, i.e., $V_{up} \sim Q^{0.3}$ (Leifer, 2010; Lemckert and Imberger, 1993). Thus V_{up} increases as plume bubbles grow or decreases as they dissolve. The upwelling flow transports bubbles upwards faster than normal and also transports CH_4-enriched, deeper water (Leifer et al., 2009). V_{up} enhances bubble survival by decreasing the rise time to the surface and by bringing bubbles to shallower depths sooner with more of their seabed CH_4 – shallower bubbles outgas more slowly than deeper bubbles from lower hydrostatic pressure (Eqn. (3)).

Strong and broad upwelling flows have been measured for several seep megaplumes in the COP seep field, offshore California in water depths from 22 to 70 m, with upwards fluid velocities (V_{up}) from ~30 cm s^{-1} to significantly greater values (Table 1). The bubble plume volume flux, Q, (discussed below) for the 22/4b seabed

Table 1
Quantified bubble megaplume seepage.

Designation	Location	Water depth (m)	V_{up} (m s^{-1})	Q($\times 10^6$ L dy^{-1})	W (m)	V_{up} citations
Trilogy	COP	45	0.30	(4.2–5.4)/3*	10	(Leifer et al., 2009)
Seep Tent	COP	70	>1	5.7*	–	(Leifer et al., 2000a)
Shane Seep	COP	22	0.30	1.1–2.6*	15	(Leifer et al., 2006)
Shane Seep Ejection	COP	22	2	6.6**	–	(Leifer et al., 2006)
La Goleta Seep	COP	70	0.30	0.8–1.2*	–	(Leifer et al., 2000a)
22/4b-4	NSea	120	>1.5	7.8***	20	(Wiggins et al., 2015)
22/4b-4 (2006)	NSea	120	1	2.8xx	15x20	(Schneider von Deimling et al., 2015)

V_{up} is upwelling flow, Q is STP volume flux (assuming no dissolution), W is plume width, COP is Coal Oil Point seep field, California. NSea is North Sea. * surface from Clark et al. (2010); ** is for the seabed from Leifer et al. (2006), a transient event; *** seabed from Leifer (2015); xx surface from Schneider von Deimling et al. (2015).

plume is considerably larger than those in the COP seep field and its V_{up} in 2010 during the quantification study (Wiggins et al., 2015) is significantly larger than values reported for COP seep field megaplumes. A least-squares linear-regression analysis was applied to derive the exponent, b, of the power law $V_{up} \sim Q^b$ from Table 1 and found $b = 0.85$ ($X = 6$, $R^2 = 0.94$, where X is the number of data points). The calculation neglected the Shane Seep ejection (a transient event likely governed by non-steady state processes) and assumes constant flux across the water column – i.e., no volume change due to gas exchange. The constant volume assumption could explain why b is steeper than the expected value of $b = 0.3$ (Lemckert and Imberger, 1993; Matsunagi and Miyanaga, 1990), although (Leifer, 2010) found good agreement ($b = 0.35$) for non-megaplume marine seep bubble plumes. A number of other factors could explain the discrepancy, including feedback from larger plumes dissolving more slowly would increase b; although, complexities such as stratification, reduce b (Leifer et al., 2009). Finally the interaction between upwelling flows and currents is complex (Leifer et al., 2015) and its effect on b largely unknown. Thus, this analysis must be considered qualitative.

Bubble plumes processes result from the integrated sum of the contribution of the individual bubbles escaping the seabed, each size class of which follows different evolutionary paths. Seabed seep bubbles escape from the seabed in a plume with an initial bubble size distribution, $\phi(r_o, z_o)$, at depth, z_o, with initial radius, r_o. As bubbles in each size class rise, their evolution is governed by Eqns. (1)–(4), leading to a depth changing bubble-size distribution, $\phi(r,z)$. This is expressed as a profile in the plume volume flux profile, $Q(z)$:

$$Q(z) = \int \phi(r,z)\frac{4\pi r^3}{3}dr \tag{5}$$

where the bubble plume molar content profile is:

$$N_i(z) = \int n_i(r,z)\phi(r,z)dr \tag{6}$$

with the plume dissolution rate is given by the depth difference, dN_i/dz.

2. Methodology

2.1. Water sampling and analysis

For several reasons (weather concerns, mechanical problems, and reduction of the campaign to a single vessel), the planned, extensive water-sampling program was reduced to collecting a limited number of water samples in and near the bubble plume using a CTD rosette sampler and the small, ROV-mounted Niskin bottles. Samples from 6 CTD casts and 7 ROV dives were collected.

Background water sample profiles were collected from three of the four corners of the study site, ~1.2 nm from the main crater to the northwest, northeast, and southeast. In addition, plume and near field water samples were collected from another three hydrocasts (Fig. 2). After the first two CTD casts, the Niskin bottles were discovered to have triggered unreliably and were transferred onto the ROV for sample collection. Eighteen ROV water samples were collected at the 22/4b-4 crater and at a secondary small crater located 1.2 nm to the southeast of the main crater (see Wilson et al. (2015) for more details on this secondary crater's plume). Samples were collected from 10-m depth to near the seabed. The deepest samples, at ~100 and 114 m, were collected within the main 22/4b crater. Vent gas samples also were collected at the seabed by the ROV into specialized airtight, Niskin bottles from a major gas plume and at the small crater plume for δ^{13}C–CH_4 analyses and $C_1/(C_2–C_4)$ ratios.

During sampling operations, both with the rosette and with the ROV, sub-sea positioning was provided using the ship's Sonardyne Ranger USBL system. Once the Rosette was recovered on-board, triplicate samples were transferred to sealed sample bottles (nominal 120 ml). Each bottle was injected with one ml of copper sulphate solution to prevent microbial CH_4 production or consumption. Of the three samples, one was injected with headspace gas and a gas sample withdrawn and analyzed to derive hydrocarbon concentrations on board. Remaining bottles were analyzed separately post mission by the University of Washington and by the Naval Research Laboratory.

Samples were analyzed by modified headspace method, described in Supp. Mater. Narrative S2. Herein, we present the water column $C_1–C_4$ data and analysis. Samples were analyzed by flame ionization detection on a gas chromatograph (SRI 8610C, SRI, Torrance, CA) configured with a 2-ml sample loop, a 15-m long Restek MXT-1 Crossbond dimethyl polysiloxane column, and a 30-m long Restek RT Alumina porous open tubular capillary column as the analytical column. Four separate calibration curves were used from 0.2 to 1000 ppmv for $C_1–C_4$ with an analytical precision of 3% for the lower concentration samples and better than 1% for the higher concentration samples.

A thorough description of the stable isotope analysis is presented in Coffin et al. (2013). Briefly, stable carbon isotope analysis of CH_4 in gas and water samples was determined using a ThermoFinnigan Trace Gas Chromatograph (GC) in-line with a ThermoFinnigan Delta Plus XP isotope ratio mass spectrometer (IRMS) via a GC-CIII combustion interface. The gas samples were directly injected into a split/splitless inlet in split mode. Water sample headspace was injected into a helium stream and cryogenically concentrated onto a 3-cm segment of Porapak-Q column (0.32 mm ID) immersed in liquid nitrogen. After focusing, the sample was rapidly desorbed onto the GC column. In both cases, CH_4 was separated on a Poraplot-Q capillary column (30 m; 0.32 mm ID) before combustion and introduction to the IRMS. The GC was run isothermally at 50 °C with a constant flow of 3.0 mL min^{-1} for gas samples, and at −10 °C with a constant flow of 2.5 mL min^{-1} for water samples. NIST Reference Material 8560 (natural gas, petroleum origin) was analyzed using the same system described above to nor-

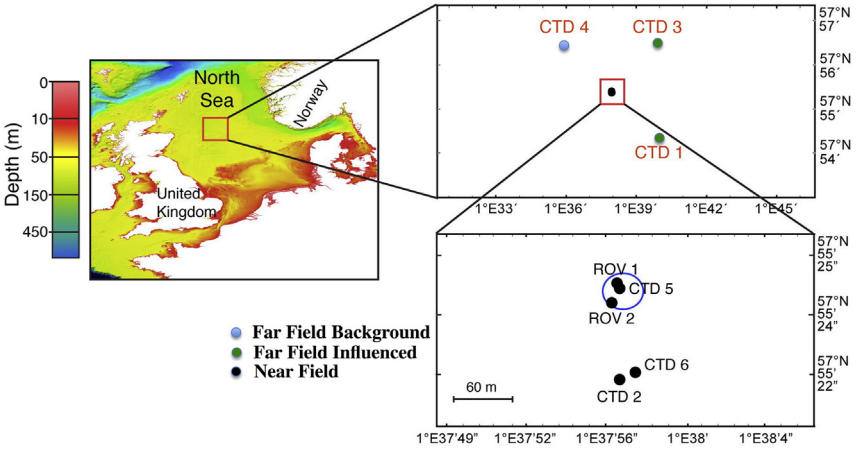

Fig. 2. Location map of 22/4b study site and water column sample locations. Blue circle shows approximate crater rim. (For interpretation of the references to color in this figure legend, the reader is referred to the web version of this article.)

malize the CO_2 reference gas. A normalization curve was generated from a linear regression of measured $\delta^{13}C$ versus standard $\delta^{13}C$ to adjust measured $\delta^{13}C$ values to the Vienna Pee Dee Belemnite (VPDB) scale.

All stable isotope ratios are reported in units of per mil (‰) using the standard notation

$$\delta^{13}C = \left[\frac{R_{sample}}{R_{Standard}} - 1\right] \times 1000 \quad (7)$$

where $R_{Standard} = {}^{13}C/{}^{12}C$ the reference standard is the VPDB scale. Values are reported with 1σ errors of replicate measurements.

2.2. Numerical bubble propagation model

The numerical bubble model solves the stiff, coupled differential equation system describing changes in bubble mass, pressure, and size and depth using a third-fourth order Runge-Kutta integration scheme Eqns. (1)–(4), which ensures numerical stability. The model has been described previously (Leifer and Patro, 2002; Rehder et al., 2009) and validated by field data (Rehder et al., 2009). A model flow chart is shown in Supp. Fig. S6.

Plume processes, specifically, V_{up} and plume aqueous concentration, C, can vary with z and t. High pressure effects on solubility and rise velocity (via density) can be simulated (Leifer et al., 2006; Rehder et al., 2009) but were neglected for these relatively shallow water simulations – their importance begins around 200 m depth (slightly shallower if significant larger hydrocarbons). Finally, this study incorporated two additional processes, enhanced bubble gas exchange and large vortical motions, which are discussed below.

Model improvements since Rehder et al. (2009) include incorporation of temperature profiles, with a number of previous scalar factors now being derived from depth-dependent lookup tables, e.g., gas solubility and diffusivity. Also new is that water density profiles are now lookup tables. For computational reasons, the radius-dependent lookup tables for V_B and k_B still are simulated as isothermal.

The model simulates each bubble size class in $\phi(r_o, z_0)$ and then interpolates the bubble gas content and gas loss (or gain) to a uniform depth grid. Bubble-size distribution profiles, $\phi(r, z)$, are calculated by re-binning $\phi(r_o, z_o)$ with the depth-evolving bubble size to the uniform depth and radius grid. The plume volume is calculated by Eqn. (5) and the bubble plume molar content profile is calculated by Eqn. (6) with the dissolution rate given by dN_i/dz.

The model can run iteratively, where on the first run, the dissolved gas concentration depth profile, $C_i(z)$, is calculated from dN_i/dz and a mixing parameter which signifies a level of injection of plume water into the ambient water and of ambient water in the plume water. In subsequent iterations the calculated $C_i(z)$ is used in Eqn. (2). In practice, convergence of $C_i(z)$ is quick, typically within three iterations (Leifer et al., 2006). A simulation for the measured dissolved plume concentrations found that plume saturation had negligible effect on flux (Eqn. (2)), even for the most conservative case of zero plume mixing with the ambient fluid. This obviated the need for iterative simulations. Note, the effect of mixing on V_{up} is implicitly incorporated by using observated V_{up} values.

3. Field measurement results

3.1. Overview

Water column CH_4 (Fig. 3C; Supp. Tables S1 and S3, Supp. Fig. S2) ranged from 5 to 99,000 nM ~2–40,000 times atmospheric CH_4 equilibrium partial pressure based on Henry's Law (Wiesenburg and Guinasso, 1979). Significantly higher CH_4 concentrations were observed consistently below the thermocline and in the bubble plume than above the thermocline. Of the seven CH_4 profiles, six included a sample above the thermocline, which always was the lowest CH_4 concentration in a profile.

3.2. Background and near-field measurements

Background CH_4 concentrations ranged from 5.3 to 68 nM (Fig. 3; Supp. Table S1, Supp. Fig. S2) with the lowest in the northwest (CTD-4) and the highest in the southeast (CTD-1). This indicates that northwest concentrations likely represent study area background concentrations (5.3–15.4 nM) while the water column at CTD-1 and CTD-3 likely were influenced by CH_4 from the 22/4b plume and/or smaller seepage identified in the survey area depending on the currents (Schneider von Deimling et al., 2015). In general, background CH_4 was highest between 70 and 85-m depth, decreasing monotonically to ~9–15 nM at depths of 30–50 m (Fig. 3; Supp. Table S1). The higher, near-seafloor concentrations coincided with nearly isothermal water (~62–85 m). In all profiles, concentrations decreased across the thermocline (Fig. 3). These contrast with near bottom-water column measurements in 2006, of 200 nM several kilometers distant from the 22/4b site (Schneider von Deimling et al., 2015); however, emissions, bubble sizes, and oceanographic factors may have been different.

Near-field water samples were collected from ~60 m south of the main crater (CTD-2, CTD-6) and ranged from 21 to 488 nM CH_4

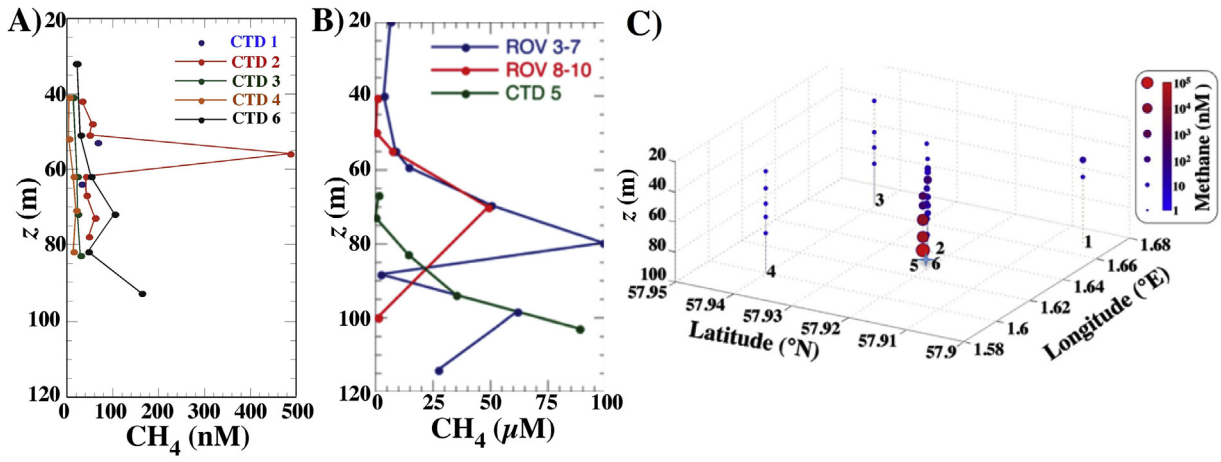

Fig. 3. Compilation of methane, CH_4, concentration profiles from the A) near-field and background and near-field locations (CTD-2, 3, 4, and 6) and B) above the main crater (CTD 5 and ROV dives). Note the different scale between the background/near-field locations and the main crater profiles. C) Spatial summary of all CTD and ROV CH_4 data. Blue star shows crater location. (For interpretation of the references to color in this figure legend, the reader is referred to the web version of this article.)

(Fig. 3; Supp. Table S1). The closest, near-field measurements to the crater (CTD-6) showed CH_4 concentrations decreasing steadily and approximately exponentially from near seabed to above the thermoline (164 nM at 93 m to 21 nM at 32 m)

A second, near-field profile slightly further south (CTD-2) showed fairly uniform CH_4 levels (34–88 nM) from ~80 to 40 m depth, except for a prominent CH_4 spike of 488 nM at 56 m (Fig. 3A; Supp. Table S1), which coincided with the thermocline base (Fig. 4). Upper water-column CH_4 concentrations from 30 to 50 m deep for CTD-2 were elevated significantly compared to the similar background depth measurements – e.g., CTD-1, 3, and 4 (Fig. 3A).

Propane was detected at trace levels at almost all depths in all profiles, except the plume profile (Supp. Tables S2 and S3). Butane also was detected at trace levels in most samples; however, ethane was not detected in the study samples. Gas samples collected from the plumes at the main crater were devoid of these higher molecular weight hydrocarbons (Supp. Table S4). The 22/4b plume measurements are consistent with the gas emitted by the 22/4b plume arising from a microbial source that lacks a thermogenic component.

3.3. Main plume measurements

Several vertical CH_4 profiles were collected for the 22/4b crater (Fig. 3C; Supp. Tables S1 and S3) where concentrations were dramatically higher than the near field – note μMol scale on Fig. 3B. For one profile, CTD-5, CH_4 crater concentrations at 103 m depth were 88,800 nM, exponentially decreasing with depth approximately exponential to 1580 nM at 67 m (Fig. 3B). This depth trend shape is similar to the concentration profile in 2006 (Schneider von Deimling et al., 2015). This strong decrease in concentrations occurs entirely below the thermocline in a depth interval of nearly isothermal seawater (Fig. 4). CH_4 concentrations in samples from the first ROV dive (ROV 3–7) were quite variable, from a few nanomolar in the upper water-column, to 99,100 nM at 80 m. This dive returned the deepest water sample at 114 m from near the crater floor with 27,500 nM CH_4 (Fig. 3C; Supp. Table S3). Above the peak at 80-m depth, CH_4 concentrations decreased sharply to ~60 m above which they were relatively constant, ranging from 3920 to 14,600 nM. The rapid decrease in CH_4 concentrations above 60 m coincides with the thermocline. The CH_4 concentration–depth profile measured during the second ROV transect (ROV 8–10) is similar to the first with a concentration maximum of 49,300 nM at 70 m and a sharp decrease in CH_4 concentrations above this depth, coincident with the thermocline. Similar sharp decreases across the thermocline were noted in 2006 by Schneider von Deimling et al. (2015). Upper water-column CH_4 concentrations directly above the main crater were ~16% of the bottom-water concentrations (Fig. 3B; Supp. Table S3), but were up to 1800 times upper water-column background values in the study area (Fig. 3A; Supp. Table S1).

The peak in CH_4 concentrations observed in both ROV transects between ~65 and 80 m is broadly consistent with the peak in CH_4 concentrations observed at 56 m in CTD-2, however the thermocline was deeper in the near-field CTD casts than in the ROV casts (Fig. 3) by ~10 m, consistent with the strong upwelling flow (Wiggins et al., 2015) lifting the thermocline locally. The ROV and CTD data suggest the plume deposits CH_4 below the thermocline with some southward CH_4 transport (i.e., downcurrent at the measurement time) towards CTD-2 (Fig. 3C).

3.4. Stable isotope analysis

Stable carbon isotope compositions were determined for dissolved CH_4 in four water-column and twelve free-gas samples. The $^{13}C_{CH4}$ values for the water-column samples range from −74.57‰ to −75.51‰, similar to values reported for gas escaping from the area by Schneider von Deimling et al. (2015). For the gas samples, $\delta^{13}C_{CH4}$ ranged from −75.6‰ to −70.7‰ (mean −74.6 ± 1.3‰) suggesting a microbial CH_4 source consistent with the non-methane hydrocarbon concentration data at the main crater. The $\delta^{13}C_{CH4}$ values for the two samples from the southeast crater are −75.6‰ and −75.1‰. Based on carbon stable isotope composition, gases from the southeast and 22/4b-4 craters are indistinguishable.

3.5. Atmospheric methane

Atmospheric CH_4 concentrations measured during the Sept. 2011 survey within 4 km of the 22/4b plume primarily were in the range 1.8–1.9 ppm (Supp. Figs. S3 and S4) with a mean of 1.85 ± 0.03 ppm and median of 1.846 ppm (see Supp. Fig. S3 for methodology). For reference, the most recent and nearest background CH_4 measurements were from Ocean Station M (2.00°E, 66.00°N) in 2009 and were 1.874 ± 0.012 ppm for the year (NOAA, 2013; http://www.esrl.noaa.gov/gmd/dv/data/?site=STM).

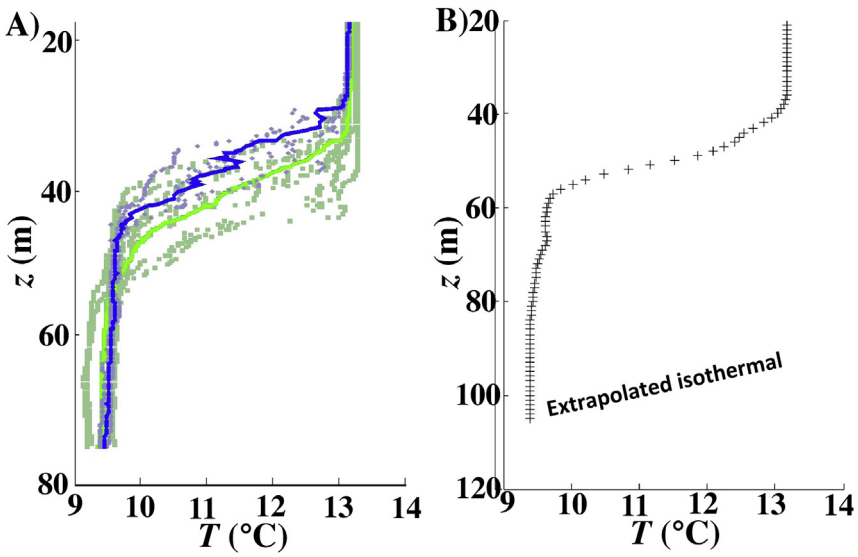

Fig. 4. A) Summary of all crater (blue) and near-field/background (green) CTD temperature, *T*, depth, *z*, profile profile data (symbols), and mean profile data (lines) for each. B) *T* profile used in bubble model. (For interpretation of the references to color in this figure legend, the reader is referred to the web version of this article.)

4. Numerical simulations

The water column CH_4 concentrations (Fig. 3) and near background atmospheric concentrations (Supp. Figs. S3 and S4) suggest negligible plume CH_4 transport out of the deeper water column. Still, even absent the upwelling flow, large bubbles should transport non-negligible CH_4 to the sea surface. For example, simulations in Leifer and Patro (2002) showed that bubbles larger than $r \sim 5000$ μm transported more than 50% of their seabed CH_4 to the atmosphere from 100 m and many bubbles this large were observed at the 22/4b site Leifer (2015). Furthermore the very strong upwelling flow (Supp. Fig. S5) discussed in Nauw et al. (2015b) and Wiggins et al. (2015) should greatly increase CH_4 transport to the sea surface, in seeming contrast to water column and atmospheric observations.

The implications of the very strong upwelling flows to water column and atmospheric CH_4 were investigated with a numerical bubble propagation model. A synthetic seabed bubble size-distribution was used for the simulations, based on the video survey in Leifer (2015) and described in Section 4.3. Table 2 summarizes key simulation parameters (complete parameter lists are in Supp. Figs. S7–S15) and the predicted fraction of direct bubble transported flux to the sea surface, Γ.

4.1. Initial conditions

Bubbles were simulated with size-varying contamination – large bubbles are clean, with clean bubbles being more efficient at gas exchange and small bubbles are dirty with a transition at $r \sim 830$ μm based on Patro et al. (2002). For these shallow waters, high-pressure effects, such as deviations in compressibility and solubility from the ideal gas law and Henry's law, respectively, were not simulated. Simulations used the mean temperature profile (Fig. 4B).

Simulations incorporated the air gases as trace components at 2%, 6%, 2%, and 1 ppm for oxygen, O_2, nitrogen, N_2, CO_2, and Argon, Ar, respectively, the balance being CH_4. Trace gases do not affect bubble fate (Leifer, 1995) but provide useful information on the importance of solubility and diffusivity to bubble gas exchange, which cannot be determined from the dominant gases that also drive volume changes. Seawater was initialized with O_2, N_2, and Ar in atmospheric equilibrium, and CO_2 at trace levels to improve initial numerical stability compared to initialization with no dissolved trace gas. The Ar initialization drives an initial bubble uptake. Bubbles have trace air (a few percent) at seabed release, which presumes bubbles absorb some air gases while traversing the near-seabed, coarse-grained sediments. This assumption may be conservative if there is significant water circulation through near surface sediments, allowing some level of sub-surface air equilibration. However, as each bubble rises in the water column, air gases rapidly diffuse into the bubbles, thus the initial bubble air gases partial pressures are not critical parameters. Argon was trace in the initial bubble gas composition to investigate the gas invasion (into the bubble) without affecting overall bubble behavior.

4.2. Single bubble simulation

Simulations of single bubbles were conducted for the observed strong 22/4b upwelling flow, $V_{up} = 1$ m s^{-1} (Table 1; Supp. Fig. S5). Although stronger V_{up} were observed (to 1.5 m/s) they did not persist with such strength across the entire water column, thus the more conservative value was used. Note, there likely are even stronger upwelling flows in the plume proper where ADCP observations are not feasible. Simulations also were conducted for a far slower upwelling flow, $V_{up} = 25$ cm s^{-1} (*run3000*, *run3001*, see Supp. Fig. S7 for simulation parameters). The latter corresponds to a bubble in a normal, megaplume bubble plume flow, such as Shane Seep (Table 1). In the megaplume (*run3000*), an intermediate size bubble with initial radius (seabed), $r_0 \sim 2200$-μm, lost ~80% of its seabed CH_4 mass by the time it reached the sea surface, while a very large bubble ($r_0 \sim 5000$ μm) lost less than 20% of its seabed CH_4 (Fig. 5A). For the lower V_{up} (*run3001*) mass loss is even greater. Overall sensitivity to V_{up} for mass loss is less for the larger, $r_0 \sim 5000$-μm bubble than for the smaller $r_0 \sim 2200$ μm bubble (Fig. 5A). The key factor is the shorter subsurface lifetime for the higher V_{up}, which decreases the time for mass loss, and also decreases the concentration difference (Eqn. (2)) sooner by bringing the bubble more quickly to shallower water where the concentration difference is less (lower hydrostatic pressure).

As bubbles rise, the air gases (O_2, N_2, Ar) diffuse into the bubbles, while CO_2, which initially was supersaturated in the bubble more rapidly outflows the bubbles due to its greater solubility (Fig. 5B). CO_2 outflow largely ceases by ~25 s, thereafter increasing slowly as the bubble grows from air inflow and decreasing hydro-

Table 2
Numerical simulation summary.

Run	Gpar	Fpar	MGas	TrGas	Bubble	V_{up}	k_{BE}	k_S	F_{SS} (L s^{-1})	Γ (%)	Comment
3000	3000	3000	CH_4, N_2	CO_2, Ar, O_2	224bSynth	100	0	1	51.8	58	Megaplume, realistic V_{up}
3001	3000	3001	CH_4, N_2	CO_2, Ar, O_2	224bSynth	25	0	1	32.8	36	Megaplume, weak V_{up}
3002	3000	3000	CH_4, N_2	CO_2, Ar, O_2	Minor1B	100	0	1	45.3	50	minor S_F = 26,482
3004	3000	3000	CH_4, N_2	CO_2, Ar, O_2	Caldera1J	100	0	1	52.6	58	major S_F = 1447
3006	3000	3000	CH_4, N_2	CO_2, Ar, O_2	ShSeep52-1	100	0	1	18.5	21	minor, S_F = 39,982
3008	3000	3000	CH_4, N_2	CO_2, Ar, O_2	ShSeep9-4	100	0	1	60.7	67	intermediate, S_F = 14,024
3009	3000	3009	CH_4, N_2	CO_2, Ar, O_2	224bSynth	0	0	1	17.3	19	No upwelling flow
3010	3010	3000	CH_4, N_2, CO_2	Ar, O_2	224bSynth	100	0	1	3.5	3.9	Dominant CO_2 bubbles
3020	3020	3000	CH_4, N_2	CO_2, Ar, O_2	224bSynth	100	2	1	10.4	12	Enhanced k_B
3021	3020	3000	CH_4, N_2	CO_2, Ar, O_2	224bSynth	100	4	1	2.7	3.0	High enhanced k_B
3022	3020	3000	CH_4, N_2	CO_2, Ar, O_2	224bSynth	100	0.5	1	34.8	39	Low enhanced k_B
3023	3020	3000	CH_4, N_2	CO_2, Ar, O_2	224bSynth	100	6	1	0.8	0.9	Very high enhanced k_B
3030	3030	3001	CH_4, N_2	CO_2, Ar, O_2	224bSynth	25	0	2	25.9	29	Slow rise
3031	3031	3001	CH_4, N_2	CO_2, Ar, O_2	224bSynth	25	0	4	20.8	23	Very very slow rise
3032	3032	3001	CH_4, N_2	CO_2, Ar, O_2	224bSynth	25	0	3	22.8	25	Very slow rise
3033	3033	3001	CH_4, N_2	CO_2, Ar, O_2	224bSynth	100	0	3	48.4	54	Very slow rise, realistic V_{up}
3040	3040	3000	CH_4, N_2	CO_2, Ar, O_2	224bSynth	100	2	2	8.5	9.4	Slow rise & enhanced k_B
3041	3041	3000	CH_4, N_2	CO_2, Ar, O_2	224bSynth	100	4	2	1.9	2.1	Slow rise & high enhanced k_B

**GPar, FPar are the Gas, and Flow parameter file numbers, see Supp. Material, Figs. S7–S15 for full parameter settings for each simulation. MGas and TrGas are major and trace gases, respectively. Bubble identifies the bubble size distribution, V_{up} is upwelling flow (cm s^{-1}), k_{BE} is the individual bubble gas exchange rate enhancement factor, see Eqn. (9), and k_S is the rise distance factor increase from vortical motions, see Eqn. (4), F_{SS} is the bubble CH_4 volume flux at the sea surface, and S_F is the scaling factor from a specific bubble plume volume to the estimated 90 L s^{-1} for the 22/4b megaplume (Leifer, 2015), and Γ is the percent of seabed CH_4 transferred to the sea surface. For 224bSynth, S_F = 1.

static pressure (Fig. 5B). By this time, CO_2 has reached equilibrium in the model.

The very strong upwelling flows (V_{up} = 1 m s^{-1}, Supp. Fig. S5) of the 22/4b megaplume allows bubbles to reach the surface much faster than for weaker upwelling flows, thereby better preserving bubble CH_4 content. In stagnant water (V_{up} = 0 m s^{-1}), large bubbles rise at ~25–30 cm s^{-1}, requiring ~5 min to reach the sea surface (not shown), rather than ~1.5 min for the very strong megaplume upwelling flow (Fig. 5D).

This intense upwelling flow allows even small bubbles to reach

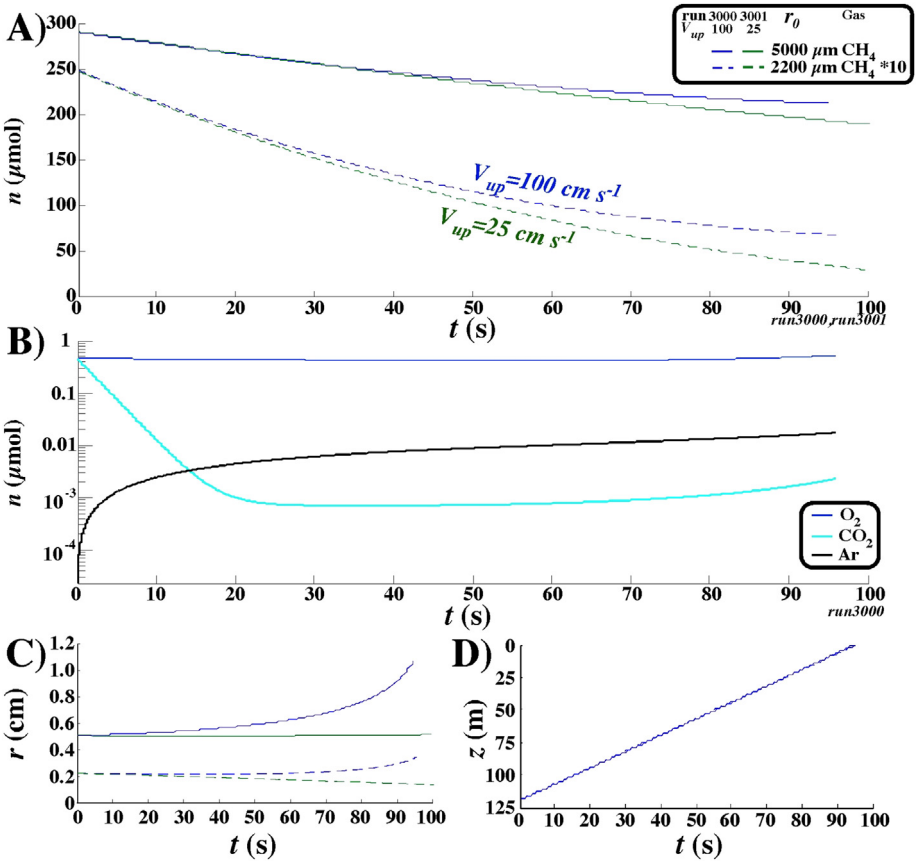

Fig. 5. Individual bubble simulations of bubble molar content, n, with time, t, for seabed or initial bubble radius, r_0 ~ 5000 and 2200 μm A) for major gas, methane, CH_4, and upwelling flow, V_{up} = 25 and 100 cm s^{-1}, (*run3000*, *run3001*, respectively), B) for minor gases with r_0 = 5000 μm and V_{up} = 100 cm s^{-1} (*run3000*). C) Trend in r for r_0 ~ 5000 and 2200-μm bubbles, V_{up} = 25 and 100 cm s^{-1} (*run3000*, *run3001*), D) Depth, z, trend for r_0 ~ 5000, 2200 μm bubbles and V_{up} = 100 cm s^{-1} (*run3000*). Data key on panels A, B.

the sea surface rather than dissolving subsurface (Fig. 6B), while decreased bubble mass loss yields larger bubbles at the sea surface (Fig. 6A). For V_{up} = 25 cm s^{-1}, only bubbles smaller than $r_0 \sim 1900$ μm dissolve sub-surface, while for V_{up} = 1 m s^{-1}, all bubbles larger than a few hundred micrometers r_o reach the sea surface. For comparison, the no upwelling case – i.e., bubbles not in a plume (*run3009*, Table 2) – showed bubbles smaller than $r_0 \sim 3000$ μm dissolved subsurface.

4.3. Bubble plume simulations

To simulate the overall fate of 22/4b megaplume CH_4, the model was initialized with Φ, the global size distribution. In the case of the 22/4b megaplume, Φ is comprised of numerous bubble plumes with different bubble plume size distributions, ϕ for the 22/4b site. Φ was estimated from the number of bubble plumes, M_j, in each plume class, j, for an assigned ϕ_j:

$$\Phi = \sum_j \phi_j M_j \tag{8}$$

Plume classes used were based on 22/4b seabed ROV observations of plume classes (Leifer, 2015) – minor, intermediate, and major, with ϕ_j after Leifer (2010), see Supp. Fig. S16 for detailed size distributions, ϕ_j and example images Values of M_j were derived from analysis of a video survey of the active seabed at 22/4b, described in Leifer (2015). The video survey analysis was based on the appearance of the bubble plumes, which then was used to classify the plume appropriately based on published field observations (Leifer, 2010) and laboratory bubble plume studies. Outside the deepsea (deeper than ~2 km) the bubble formation size distribution should be independent of pressure because the water-bubble density difference is close to unity. This explains the similarity between minor plumes at depths of 1 km and in the shallow Coal Oil Point seep field at 20-m depth (Leifer, 2010).

Specifically, representative bubble plume ϕ from the Coal Oil Point seep field, offshore California (Fig. 7) were selected for the three classes – listed in Leifer (2010; Table 1) as "Caldera J", "ShSeep9-4", and "Minor1B" (with *recalculated* values of buoyancy flux or plume volume, Q, of 62.2, 6.315, and 3.4 cm^3 s^{-1}, respectively). Only non-oily plumes were considered.

Minor bubble plumes have ϕ that is well described by a Gaussian function with peak size solely related to orifice size (grain spacing) below a critical flow rate, such that increased flux increases the bubble emission frequency. Above the critical flow rate, the peak size increases with flow (Leifer and Culling, 2010). Major bubble plumes are highly turbulent, involve bubble shattering and tearing, with ϕ described by a power law whose slope relates to flux (Leifer, 2010; Leifer and Culling, 2010). Intermediate bubble plumes have characteristics of both minor ϕ and major ϕ plumes.

Each bubble size class in each plume class ϕ shown in Fig. 7 was simulated for 22/4b conditions with ϕ scaled by a scaling factor, S_F, such that Q for each plume was 90 L s^{-1}, the best estimate 22/4b seabed flux (Leifer, 2015). For major, intermediate, and minor plumes, S_F = 1447, 14,024, and 26,482, respectively. To prevent small r_0 variations in $\phi(r_0)$ from propagating into flux calculations and upper water column concentrations, $\phi(r_0)$ was smoothed by applying a nearest neighbor average, and then interpolated to twice the r_0 resolution by cubic-spline interpolation. Nearest neighbor smoothing was used to remove small fluctuations in $\phi(r_0)$ that largely arise from the radius-binning scheme used to calculate ϕ (Leifer, 2010). The interpolation better fills out calculated parameters like bubble molar content for bubble behavior that diverges with r – i.e., small bubbles dissolving and large bubbles growing.

The layer mass flux distribution, F_L, or the flux into (or from) a layer with respect to bubble size and was derived from the product of the number of bubbles in each size class, $\phi(r_0)$, and the depth derivative of the bubble molar content, $n_i(r)$ for gas i and is:

$$F_{L,i}(r_o, z) = \int_{z_1}^{z_2} \frac{\phi(r_o) dn_i(r_o)}{dt} dz \tag{9}$$

where n_i is the bubble-mediated transport (content) of gas i, and its change with time is the layer mass flux distribution, $F_L(r_0, z)$, with units of mol μm^{-1} m^{-1} s^{-1}. F_L was calculated for 1-m layers (z_2–z_1 = 1 m). For non-trace seep gases, like CH_4, F_L generally describes bubble outflow or dissolution, while for air gases; it generally describes bubble inflow (absorption or uptake) from the water column into the bubbles and is negative.

Although minor bubble plumes span a narrow radius range (Fig. 7), differences in their fate manifest even across their size range (Fig. 8A). Initially, smaller bubbles are more important to dissolution, but as they lose mass, they become less important both to dissolution and to transport higher in the water column. This manifests as a tilt or skew towards larger r_0 (Fig. 8B). The most important bubble size for minor plume mass transport is $r_0 \sim 4000$ μm, whose bubbles lose slightly less than half their seabed CH_4 by the sea surface, while $r_0 \sim 3500$ μm is most important for dissolution. Note, Fig. 8 shows bubble CH_4 molar content and dissolution with

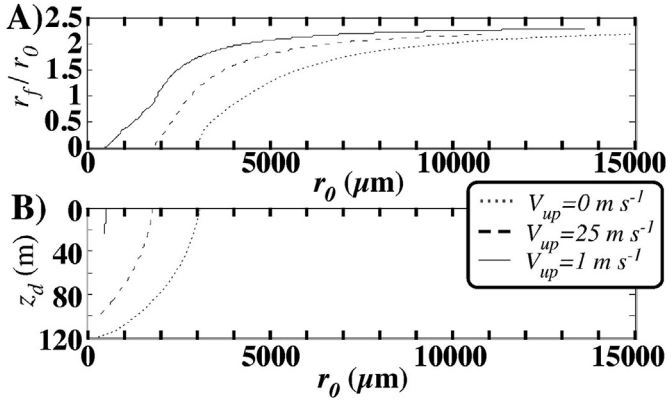

Fig. 6. A) Ratio of final, r_f, to seabed, r_0, bubble radius, showing bubble growth from seabed to sea surface, and B) bubble dissolution depth, z_d. Simulations for upwelling flow, V_{up}, of 0, 25, and 100 cm s^{-1}, Data key on figure. *run3000*, *run3001*, and *run3009*, respectively.

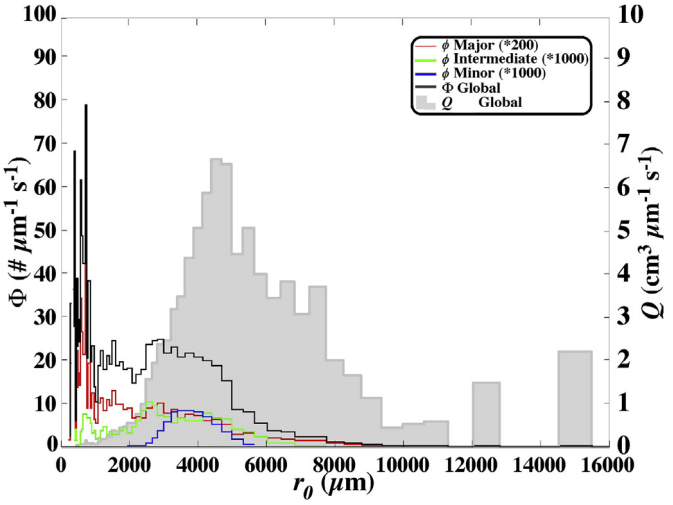

Fig. 7. Bubble size distribution, ϕ, of representative Major, Intermediate, and Minor class bubble plumes, synthesized global size distribution, Φ, and volume emission distribution, $Q(r_0)$. Data key on figure.

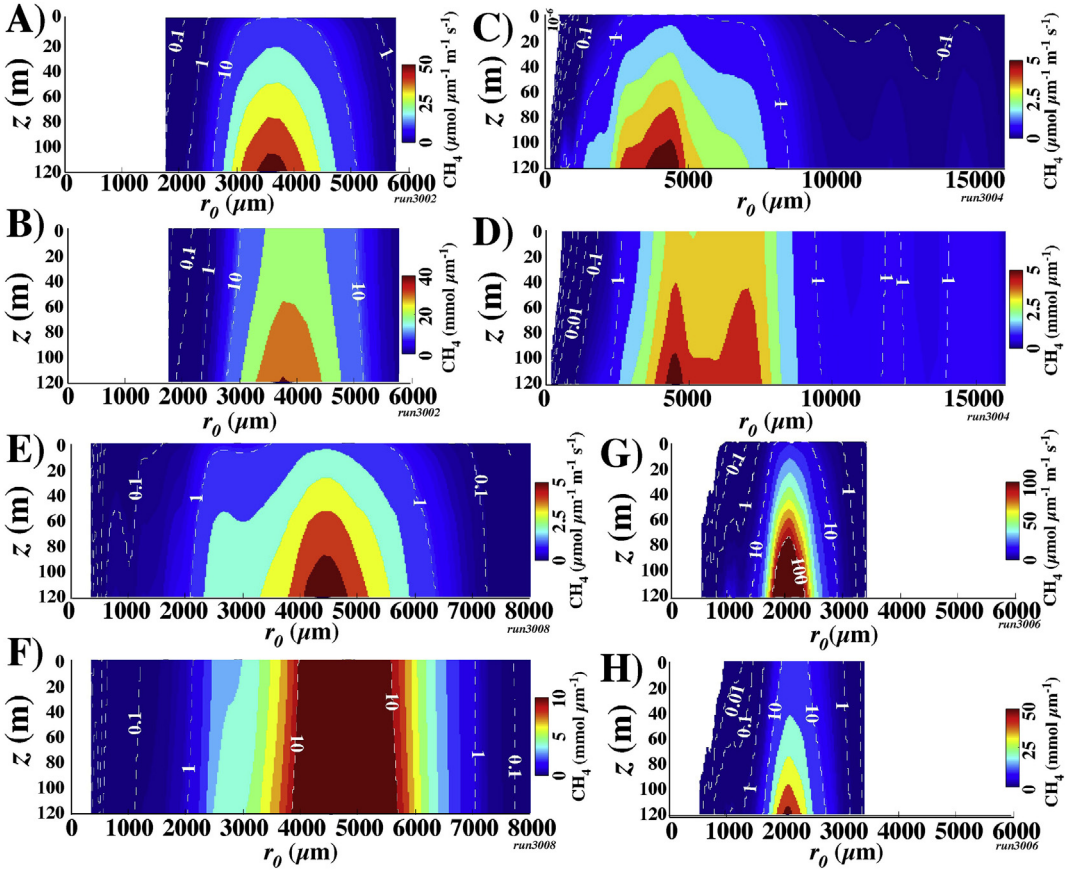

Fig. 8. Bubble plume methane, CH_4 molar content at depth, z, and dissolution rate (mass per second per radius unit deposited in a 1-m thick layer), with respect to seabed radius, r_0, and z for representative plume classes, A, B) minor plume (*run3002*), C, D) major plume (*run3004*). E, F) intermediate plume (*run3006*), and G, H) a smaller, minor plume (*run3008*). Upwelling flow was 1 m s^{-1}. Full simulation parameters available in Supp. Figs. S8 and S9. Data keys on figure. Labeled contours are decadal.

respect to seabed radius, r_o, although r evolves as the bubbles rise.

Although most major-plume bubbles (Fig. 7) were small ($r_0 < 1000$ μm), the small bubble contribution to CH_4 content (i.e., transport) and dissolution was negligible (Fig. 8C and D). Bubbles in the range $3000 < r_0 < 7500$ μm were most important to transport and dissolution, with the smaller bubbles in this range initially contributing more towards dissolution. However, as these smaller bubbles lose their mass, progressively larger bubbles (with more remaining mass) became more important, manifesting as a tilt towards larger r_0. Although few in number, very large bubbles ($r_0 > 8000$ μm) are particularly important in the upper water column, losing a far smaller fraction of their (initially far larger) seabed CH_4 than the dominant bubble size range, $3000 < r_0 < 7500$ μm. Given that these large bubbles lose only a small fraction of their seabed mass, contours for F_L are nearly vertical (Fig. 8D), with the major plume transferring $\Gamma = 58\%$ of the seabed Q to the atmosphere (*run3004*, Table 2).

The intermediate plume shares aspects of minor and major bubbles and exhibited dominant dissolution for $r_0 \sim 4500$ μm (Fig. 8E), with slightly larger bubbles dominating mass transport (Fig. 8F). Like the major plume, its larger bubbles (to $r_0 > 7000$ μm) contribute non-negligibly to dissolution in the upper water-column; however, its largest bubbles are smaller than the major plume's and are too few in number to contribute significantly to the plume's bubble mass transport.

These plumes all transport a significant fraction of their seabed CH_4 to the sea surface, far more than suggested by the water column and atmospheric observational data. A simulation of the smallest minor bubble plume measured in the Coal Oil Point seep field (Fig. 8G and H) with peak ϕ at $r_0 \sim 2020$ μm and $Q = 2.25$ cm^3 s^{-1} – $S_F = 39{,}982$ (Leifer, 2010) – predicted significantly less sea surface CH_4 than the representative minor plume ($\Gamma = 21\%$ versus $\Gamma = 50\%$, for *run3006*, *run3002*, respectively, Table 2). For this smallest minor plume, CH_4 is deposited even closer to the seabed; however, even this smaller minor plume transports to the thermocline about a quarter its seabed CH_4. This plume should be considered a minimal size distribution seep plume.

The underlying mechanism for these high transfer efficiencies is the very strong V_{up}, which, we investigate through numerical bubble plume modeling. The simulations explore processes that we hypothesize can explain how in the face of such high expected transfer efficiencies, CH_4 remains largely constrained to the deeper water column.

4.4. Global bubble megaplume simulation

To simulate numerically the 22/4b bubble plume, the model was initialized with Φ calculated by Eqn. (8) and each bubble size in Φ simulated was scaled so that $Q = 90$ L s^{-1} (Leifer, 2015). Φ was relatively flat from $1000 < r_0 < 5000$ μm then decreased sharply by over an order of magnitude by $r_0 \sim 7000$ μm. Although Φ had few very large bubbles (from the major plume size distribution, Fig. 7), they contribute significantly to $Q(r_o)$ (Fig. 7).

Overall, larger bubbles grow and smaller bubbles shrink as the bubbles rise (Fig. 9), thus, $\phi(r, z)$ near the sea surface is broader than at the seabed. By the thermocline, many small bubbles already have dissolved while the seabed bubbles at the 500 μm peak are just r_0 ~100–200 μm here. Bubbles this small and

smaller likely are susceptible to detrainment into an intrusion layer, a feature identified in hydroacoustic data (Schneider von Deimling et al., 2015; Wilson et al., 2015); however, the contribution of these small bubbles to plume mass transport or volume flux – i.e., the buoyancy driving the upwelling flow – and dissolution fluxes are negligible. Thus, detrainment was not simulated.

There is significant bubble growth in the upper few tens of meters from the rapid decrease in hydrostatic pressure (Fig. 9B). For example, bubbles at the thermocline in the range $2000 < r < 5000$ μm grow to $5000 < r < 10{,}000$ μm by the sea surface. For the smallest seabed bubbles ($r_0 < 300$ μm), complete dissolution occurs in a few tens of meters, while for $400 < r_0 < 2000$ μm, shrinkage shifts to growth at $z \sim 20$ m as decreasing hydrostatic pressure and air inflow overwhelm CH_4 outflow (which continues, albeit more slowly as the internal pressure that drives CH_4 outflow decreases (Eqn. (2)).

Small ($r_0 < 500$ μm) bubbles rapidly lose CH_4 (Fig. 10A and B), largely dissolving within the crater. These bubbles are unimportant to the overall plume mass and the fate of plume CH_4. The largest contribution, both to CH_4 transport (Fig. 10A) and dissolution (Fig. 10B) is from bubbles in the range $3000 < r_0 < 5000$ μm, which still retain significant CH_4 at the sea surface. These bubbles have slightly less than doubled in size by the sea surface (Fig. 9A).

In all (non-dissolving) bubbles, nitrogen increases (Fig. 10C), although the increase is gradual (near vertical contours) as bubbles were initialized with a few percent nitrogen (Supp. Figs. S7–S15). To understand better the factors driving air uptake, argon was simulated for trace initial bubble partial pressure and minimal water column concentration. In the simulation, bubble Ar increases rapidly, with inflow (absorption) strongest for $r_0 \sim 4000$ μm in the upper water column (Supp. Fig. S17). The peak in r_0 in dissolution flux and in molar content was similar for all the other gases. However, N_2 uptake, which also was greatest at the sea surface, was far less strongly depth-dependent than for Ar (Fig. 10C).

The importance of solubility is illustrated by comparison with the more soluble gas CO_2, whose bubble content decreases far faster than that of CH_4 (Fig. 10D). Although dominant CO_2 plumes are not relevant for 22/4b, they are investigated in Supp. Figs. S20–S22.

The profile total plume dissolution rate, $F_{L\_CH4}(z)$, for Φ can be compared to the near-field, vertical CH_4 profile (Fig. 3B, CTD-5) if one assumes depth-invariant currents and minimal upwelling fluid transport. Whether this is a realistic assumption depends on current strength, among other aspects. For strong currents, the length of time that fluid remains in the plume is short, and thus the upwelling flow distortion or lifting of deeper water towards shallower depths is minimal. For example, for a 1 m s^{-1} current and a 15-m diameter momentum plume, an upwelling flow of 1 m s^{-1} will lift fluid on average ~10 m (RMS of 15 m) – i.e., downcurrent water-column concentrations reflect bubble plume dissolution from ~10-m deeper. Obviously, this assumption is less appropriate for weaker currents and larger megaplumes. In principle, the downcurrent concentration profile, $C(z)$ can be calculated from $F_{L\_CH4}(z)$ if the current and aqueous plume eddy diffusion rates are known; however, herein we simply compare qualitatively.

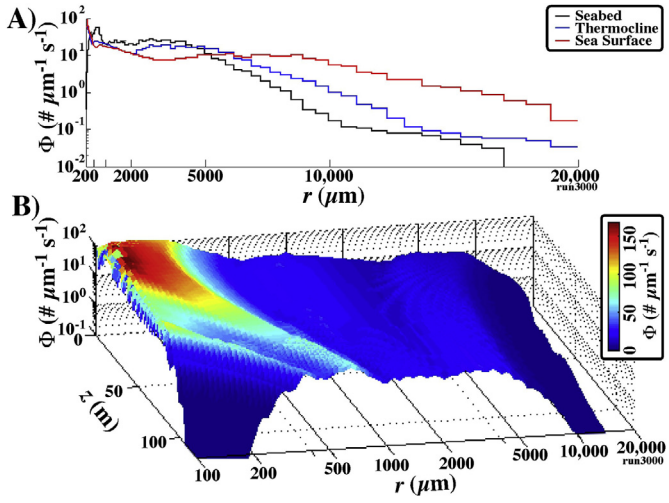

Fig. 9. Global bubble size emission distribution, $\Phi(r)$, where r is bubble radius, A) at the seabed, thermocline (40 m), and sea surface. B) $\Phi(r, z)$, where z is depth. Data key on figure.

For high upwelling flow, F_{L_CH4} decreased an order of magnitude from the seabed to the sea surface (Fig. 11B); however, less than a third of the seabed bubble N_{CH4} was lost during transit to the sea surface (Fig. 11A), with a fraction transported to the sea surface of $\Gamma = 58\%$ (*run3000*, Table 2). F_{L_CH4} decreases suddenly at ~50 m depth, corresponding to where bubbles in the important Φ peak at $r_0 \sim 3500$ μm have lost most of their CH_4 (Fig. 10A) and no longer contribute significantly to F_{L_CH4} or N_{CH4}. The only observed CH_4 depth profile, $C(z)$, that even bears some resemblance to the predicted outflow is CTD-5 (Fig. 2B), where $C(z)$ decreases exponentially by two orders of magnitude by 70-m depth, in contrast to the approximately linear decrease in F_L by a factor of ~2 for this simulation (Fig. 11B).

Sensitivity of the fate of bubble CH_4 to V_{up} was investigated by simulating Φ for $V_{up} = 25$ cm s^{-1} (*run3001*). Note, this scenario is unsupported by upwelling flow observations (Supp. Fig. S5) near the bubble plume (momentum plume), which likely were slower than fluid motions in the bubble plume (Wiggins et al., 2015).

The slower V_{up} decreased CH_4 transport to the upper water-column greatly (Fig. 12A) compared to the higher V_{up} (Fig. 10A), transporting $\Gamma = 36\%$ to the atmosphere (*run3001*, Table 2). Transport and dissolution are driven primarily by the dominant bubble peak, $3000 < r_0 < 5000$ μm, although there is greater skew towards larger r_0 in CH_4 dissolution and mass content (Fig. 12) compared to strong upwelling (Fig. 10). Significant CH_4 still is transported to the upper water column; however, the relative importance of large and very large bubbles is enhanced compared to the simulation with a stronger upwelling flow (Fig. 12A versus Fig. 10A). The decreased CH_4 transport to the upper water column is matched by the greater overall dissolution flux (Fig. 12D) compared to the higher upwelling flow simulation (Fig. 11B). The slower rising bubbles also allow more time for air gases to diffuse into the bubble, leading to higher air gas molar content at the sea-surface (Fig. 10C versus Fig. 12C; Supp. Fig. S17 versus S18C).

In the total absence of an upwelling flow, $V_{up} = 0$ m s^{-1} (*run3009*), transport to the atmosphere decreases dramatically, to $\Gamma = 19\%$ (*run3009*, Table 2) with far greater sensitivity to V_{up} between 0 cm s^{-1} and 25 cm s^{-1} than between 25 cm s^{-1} and 100 cm s^{-1}. This arises because although increasing V_{up} from 0 cm s^{-1} to 25 cm s^{-1} significantly impacts on bubbles in the most important size range, $3000 < r_0 < 7000$ μm, it only minimally affects very large bubbles, while $V_{up} = 100$ cm s^{-1} strongly affects even very large bubbles (Supp. Fig. S19 compares mass content and transport for $V_{up} = 0$, 25, and 100 cm s^{-1}).

4.5. Bubble megaplume vortical motions

Hydroacoustic and visual observations indicate the presence of large and strong vortical (spiral) motions in the plume with an approximate tilt of ~45° (Schneider von Deimling et al., 2015). These spiral motions increase the water-column transit time of bubbles, which continue rising at their normal speed while trapped in the vortical motions. This process was simulated by reducing the bubble rise velocity to V_B/k_S, where k_S is the slow-rise scaling factor,

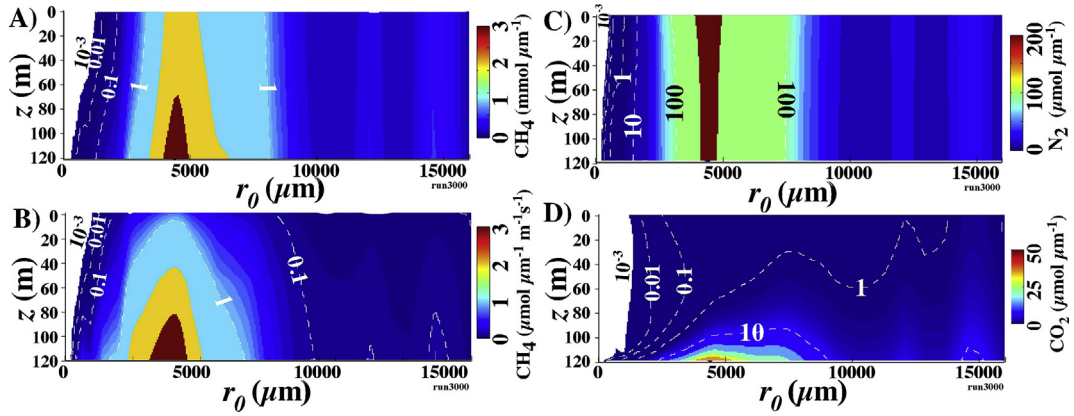

Fig. 10. A) Bubble plume methane, CH_4 molar content at depth, z, and dissolution rate (mass per second per radius unit deposited in a 1-m thick layer) with respect to seabed radius, r_0, and depth, z, for global bubble plume Φ, and strong upwelling flow. B) CH_4 dissolution rate. C) Nitrogen, N_2, content. D) Carbon dioxide, CO_2, content. Decadal contours are labeled, 10 color levels per decade. Data key on figure. (For interpretation of the references to color in this figure legend, the reader is referred to the web version of this article.)

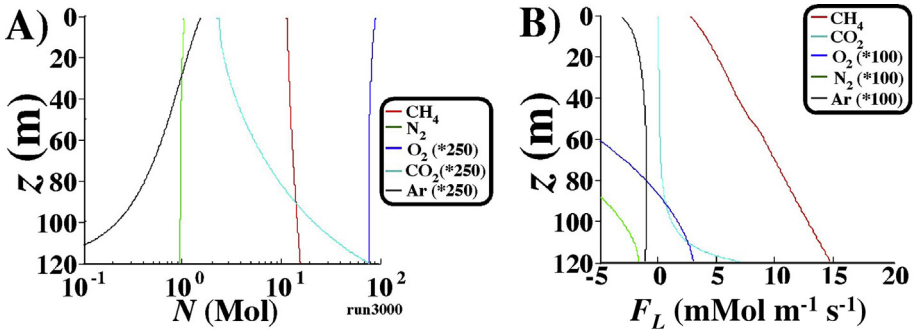

Fig. 11. Size-integrated global 22/4b bubble plume for a strong upwelling flow of 100 cm s^{-1}. A) Plume molar content, N. B) Plume gas outflow (dissolution), F_L. Outflow (dissolution) is positive, inflow (absorption) is negative. Data key on figure. *run3000*.

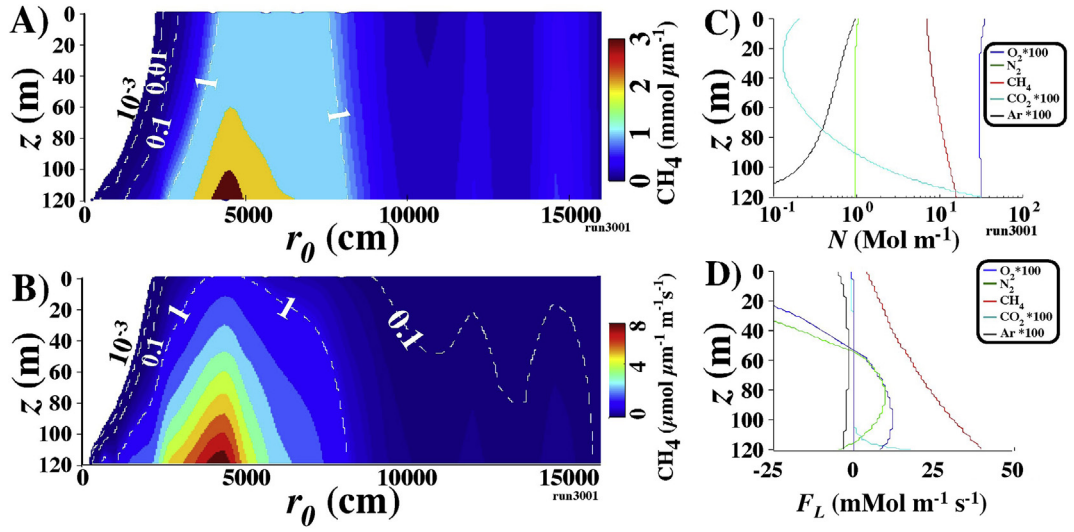

Fig. 12. A) Bubble plume methane, CH_4 molar content at depth, z, and dissolution rate (mass per second per radius unit deposited in a 1-m thick layer) with respect to seabed radius, r_0, and depth, z, for global bubble plume Φ, and a 25 cm s^{-1} upwelling flow. B) CH_4 dissolution flux. C) Size-integrated z-profile of bubble molar content, N. D) Size-integrated, z profile of plume gas flux, F_L. Decadal contours are labeled, 10 color levels per decade. Data key on figure. *run3001*. Molar content of Ar, N_2, and CO_2 in Supp. Fig. S17. (For interpretation of the references to color in this figure legend, the reader is referred to the web version of this article.)

while maintaining their normal rise speed-dependent gas transfer rate – i.e., k_B remains a function of V_B not V_B/k_S. In addition, the upwelling flow lifts the vortices and their trapped bubbles. Thus, the bubble vertical velocity, V_Z, is:

$$V_Z(r) = V_{up} + \frac{V_B(r)}{k_S} \tag{10}$$

Simulations were conducted for a range of k_S = 1, 2, 3, 4 and for V_{up} = 25 cm s^{-1} to investigate for emphasized conditions the effect of slow rise from large vortices on CH_4 fate (Fig. 13). Also a more realistic simulation was run for k_S = 4 and V_{up} = 100 cm s^{-1}. The slow rise process is distinct from the slower V_{up} simulation (Fig. 12), as slow rise affects different bubble sizes differently than

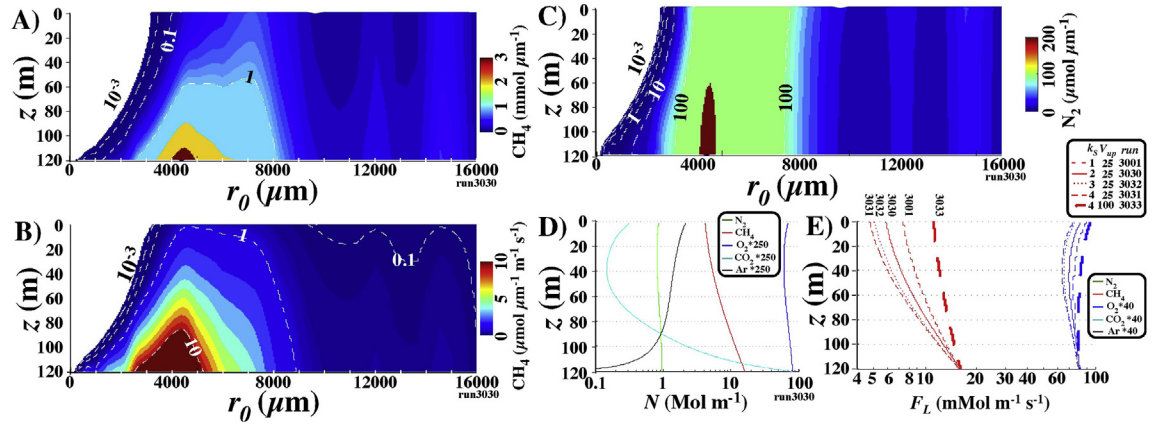

Fig. 13. A) Bubble plume methane, CH_4 molar content at depth, z, and dissolution rate (mass per second per radius unit deposited in a 1-m thick layer) with respect to seabed radius, r_0, and depth, z for global bubble plume Φ, and upwelling flow, V_{up} = 25 cm s^{-1} with slow rise factor k_S = 2, B) CH_4 dissolution flux. C) Nitrogen, N_2, bubble molar content. Decadal contours are labeled, 10 color levels per decade. D) Size-integrated z-profile of bubble molar content, N, for k_S = 2 and V_{up} = 25 cm s^{-1}. E) and dissolution rate, F_L, for k_S = 1, 2, 3, 4, and V_{up} = 25 and 100 cms^{-1} for CH_4 (red) and O_2 (blue). See data key. Only dissolving gases shown. See Supp. Fig. S23 for CH_4 and N_2 molar content for all slow rise simulations. (For interpretation of the references to color in this figure legend, the reader is referred to the web version of this article.)

slower V_{up}, skewing importance towards larger bubbles.

A comparison of simulations for k_S = 2 (Fig. 13, Supp. Fig. S23A) with k_S = 1 (i.e., run3001, Fig. 12) shows that slow rise decreases significantly sea surface bubble CH_4 molar content while enhancing overall CH4 dissolution primarily in the deeper water column. The slow rise impact is greatest for smaller bubbles with higher dissolution across the water column. Nitrogen inflow (Supp. Figs. S23E-S23G) decreases with increasing k_S (slower rise), with changes primarily for bubbles in the range, 3000 < r_0 < 6000 μm. For a stronger implementation of slow rise (i.e., slower slow rise or greater k_S) the importance decreases because bubble rise still includes the upwelling flow (Fig. 13E). As a result, the impact is greatest on smaller bubbles, which dissolve at deeper depths than for no slow rise (run3001, Fig. 12). Still, the larger bubble population is decreased significantly compared to the same upwelling flow and no slow rise (Fig. 14A). In this simulation, smaller bubble concentrations (r < 1000 μm) are comparable at the seabed and sea surface; however, larger bubbles decrease by an order of magnitude for strong enhanced slow rise (k_S = 4) compared to no slow rise (k_S = 1). Thus, slow rise shrinks intermediate to large (3000 < r_0 < 5000 μm) bubbles that would have grown from decreasing hydrostatic pressure in its absence.

Bubble CH_4 molar content decreased by a factor of about three for k_S = 2 between the seabed and sea-surface (Fig. 13D), transporting just Γ = 29% of seabed CH_4 to the sea surface compared to an absence of slow rise, where Γ = 36% (run3030, run3001, Table 2) for weak upwelling flow, V_{up} = 25 cm s^{-1}. As k_S increases, dissolution increases, depositing more CH_4 in the deeper water column (Fig. 13E); however, reasonable k_S values (k_S = 2, 4, implying approximate spiral trajectories of 45° and 22.5°, respectively) cannot reproduce observations. Although slow rise enhances greatly small bubble dissolution, it only slightly enhances large bubble dissolution.

These simulations were conducted with a slow upwelling flow (V_{up} = 25 cm s^{-1}) to magnify the effect of the slow rise process. A comparison for k_S = 4 with V_{up} = 25 and 100 cm s^{-1} (run3031 and run3033) shows the higher V_{up} increases CH_4 molar transport to the sea surface Γ = 54% compared to Γ = 23%. Thus the strong V_{up} at 22/4b largely overwhelms slow rise even for k_S = 4 (Fig. 13E; Supp. Fig. S23C versus S23D) – i.e., strong V_{up} ameliorates the impact of spiral motions.

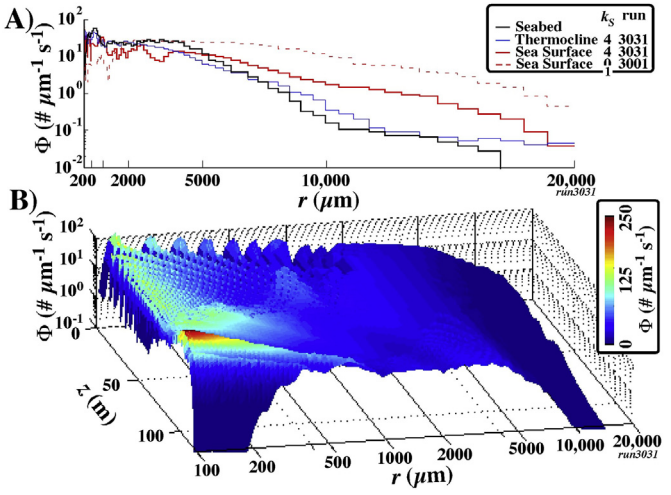

Fig. 14. Global bubble size emission distribution, $\Phi(r)$, for strong slow rise (k_S = 4) and slow upwelling flow (V_{up} = 25 cm s^{-1}), where r is radius A) at seabed, thermocline, and for no slow rise (k_S = 0) same V_{up}. B) $\Phi(r, z)$, where z is depth across the water column for k_S = 4 and V_{up} = 25 cm s^{-1}. Data key on figure. *run3031*, *run3001*.

4.6. Enhanced megaplume bubble gas exchange

Other possible explanations for the unexpectedly poor transport of seabed CH_4 to the mixed layer and atmosphere were considered and rejected, such as an unidentified highly soluble gas (not CO_2) or significant bubble fragmentation and then massive detrainment of small fragmented bubbles at the thermocline. Bubble fragmentation requires intense turbulence (Ravelet et al., 2011), which has been identified only for turbulence jets such as during wave breaking (Deane and Stokes, 2002) or high flow emissions from a vent orifice (Leifer and Culling, 2010). However, such turbulence jets were not observed in the sonar data (Wilson et al., 2015).

Thus, an alternate hypothesis was developed, based on assuming that bubble mass loss in very intense bubble plumes is greater than in normal (smaller) plumes due to externally imposed turbulence. Specifically, bubble wakes can persist for up to minutes, and as a result, in a megaplume, bubbles rise through a tangle of turbulence from persistent wakes, which have size scales comparable to the bubble boundary layer. We hypothesize that the turbulence field then enhances k_B above that for bubble self-ventilation from rise in stagnant water.

The enhanced bubble gas exchange hypothesis was investigated

in numerical simulations by introducing an enhanced individual bubble gas exchange coefficient, k_{BE}, which was simulated as r-independent and was added to $k_B(r)$. For each gas, the product of k_{BE} and the maximum value of $k_B(r)$ was added to $k_B(r)$ to generate a new bubble gas transfer coefficient, k_{BNi}, for gas i, for use in Eqn. (2) in the model:

$$k_{BNi} = k_{BE} * \max\{k_{Bi}(r)\} + k_{Bi}(r) \quad (11)$$

For $k_{BE} = 2$, the effect on the vertical profile is dramatic, with significant mass loss well below the thermocline by all bubble sizes including very large bubbles (Fig. 15). The bubble size range for complete dissolution extends to far larger bubbles (~3000 μm) than in its absence (~500 μm, Fig. 10). Interestingly, air gases both inflow and then outflow the bubble far more rapidly (Supp. Fig. S24). Specifically, N_2 initially rapidly inflows larger ($r_0 \sim$ 4000 μm) bubbles, but shifts to outflow at $z \sim 55$ m as rapid CH_4 outflow forces bubble shrinkage. The effect of bubble size change is significant for $k_{BE} = 2$, with subsurface dissolution of bubbles with $r_0 < 3000$ μm and is dramatic for $k_{BE} = 6$, with a several order of magnitude decrease across the entire bubble size distribution at the sea surface (Supp. Fig. S25). For $k_{BE} = 2$, bubbles as large as 500 μm dissolve within the crater, while larger bubbles ($r_0 \sim 5000$ μm) first shrink significantly before growing in the upper water column.

Based on the bubble molar content depth profiles (Fig. 15D), $k_{BE} \sim 6$ predicts direct bubble-mediated transport to the sea surface to levels comparable observational constraints, i.e., $\Gamma = 0.9\%$ (run3023, Table 2). Interestingly, nitrogen first inflows then outflows bubbles in the range $3000 < r_0 < 6000$ μm in the bottom water column, forming an enhanced layer between 80 and 100 m depth (Supp. Fig. S24B). The same enhanced layer is observed in the argon simulation (Supp. Fig. S26C).

A simulation for moderate $k_{BE} = 2$ and $k_S = 2$, i.e., extended residence time from vortex trapping combined with turbulence-enhanced bubble gas exchange and strong V_{up} also constrained CH_4 sufficiently to the lower water column (Fig. 16). Sea surface CH_4 is reduced dramatically with respect to simulations absent these megaplume processes (Fig. 16C) by about an order of magnitude ($\Gamma = 8\%$). For stronger $k_{BE} = 4$ and $k_S = 2$, further significant reductions in CH_4 upper water-column transport occurs, with only $\Gamma = 2.1\%$ (run3041, Table 2). This reduction in transport efficiency; however, is not accompanied by a similar reduction in the sea surface bubble size distribution for larger bubbles because faster air absorption largely compensates for faster CH_4 dissolution (Supp. Fig. S27). Interestingly, thermocline bubble concentrations are lower than at the sea surface in the size range $5000 < r_0 < 12{,}000$ μm (Supp. Fig. S27A). Specifically, the overall plume buoyancy, Q, decreased to 20% of the seabed value at 60-m depth, before growing back to 80% of the seabed Q at the sea surface.

5. Discussion

5.1. Upper-water column and atmospheric observations

Remote sensing constraints on the atmospheric plume (Gerilowski et al., 2015) and water-column data (Fig. 3) indicate that the 22/4b seabed CH_4 emissions largely were constrained below the thermocline during the fall field campaign – very little CH_4 was observed in the upper water-column. Although water-column data are sparse, they are consistent with the extensive atmospheric data (Supp. Figs. S3 and S4) that limits CH_4 transport to the upper water column (direct and indirect) and to the atmosphere. They also are consistent with other survey observations for the 22/4b site (Schneider von Deimling et al., 2015), although seabed bubble emissions only were characterized during the fall 2011 campaign.

Lower water-column CH_4 profiles were fairly uniform in character (Fig. 3) and significantly lower above the thermocline than below. This could indicate strong vertical mixing of detrained plume fluid, with thermocline detrainment forming an intrusion layer, a conceptual model that is consistent with the sonar bubble observations (Schneider von Deimling et al., 2015; Wilson et al., 2015). Given the sharpness (~10 m) of the thermocline, the thinness of the sonar bubble-outlined intrusion layer, and the coarseness of the profile sample depths, other profiles could have missed the intrusion layer (Fig. 3).

Upper water-column CH_4 concentrations from 30 to 50 m deep for CTD-2 were elevated significantly compared to the similar background depth measurements – e.g., CTD-1, 3, 4 (Fig. 3). This could result from transport of plume-deposited CH_4 in shallower depths followed by advection towards the CTD cast. Overall, even near-field shallow water-column enrichment was minimal.

The pervasive trace propane and n-butane throughout the study area (despite CH_4 spanning a very wide range of concentrations) suggests thermogenic gas sources (natural seepage or anthropogenic) outside the 22/4b site. Such additional sources also could explain the elevated "background" CH_4 concentrations for the 22/4b site compared to typical ocean values of 2–4 nM (Reeburgh, 2007; Solomon et al., 2009; Watanabe et al., 1995) and for the North Sea (Rehder et al., 1998).

5.2. Numerical simulations to explain observational constraints

Bubble plume CH_4 transport occurs by two mechanisms, directly in bubbles and indirectly in plume-transported or upwelled fluid that is enriched by bubble CH_4 dissolution (Leifer et al., 2009). Observations indicate that neither mechanism significantly transported CH_4 vertically to the upper water column or atmosphere. In terms of indirect transport, stratification can lead to massive plume detrainment, depositing much of the CH_4 in an intrusion layer (Asaeda and Imberger, 1993). The intrusion layer should form in or at the base of the (very strong) thermocline (Fig. 4) that is typical for the Central and Northern North Sea conditions in the summer and fall (Nauw et al., 2015a; Otto et al., 1990). However, stratification does not affect direct, i.e., bubble-mediated, CH_4 transport.

Thus, for this megaplume rising from fairly shallow water, the lack of a significant atmospheric CH_4 plume or upper water-column CH_4 enhancements requires that the bubbles do not transport CH_4 to the upper water-column. The lack of significant direct bubble transport is consistent with acoustic observations showing a strong diminution of the plume in upper waters compared to near the seabed (Schneider von Deimling et al., 2015; Wilson et al., 2015) and visual surface observations (Peter Linke, personal observation, 2013), which indicated only a weak and sparse bubble plume at the sea surface. Further supporting the interpretation that most bubbles did not reach near sea-surface waters for stratified conditions in fall when the survey occurred, are the upwelling data (Supp. Fig. S5) that show the upwelling flow did not reach the sea surface (Nauw et al., 2015b; Wiggins et al., 2015). Thus, the primary conclusion that bubbles are not directly transporting CH_4 to the sea surface is supported by multiple datasets, yet appears to be in contradiction with megaplume observations in the Coal Oil Point seep field, where bubbles rise from comparable depths (~70 m) and retain a significant fraction of their seabed CH_4 at the sea surface (Clark et al., 2010).

Also puzzling is that the seabed emissions estimate for the 22/4b megaplume shows it to be the strongest seabed bubble megaplume quantified to date and that it was comprised of bubbles spanning a wide size range at the seabed including many very

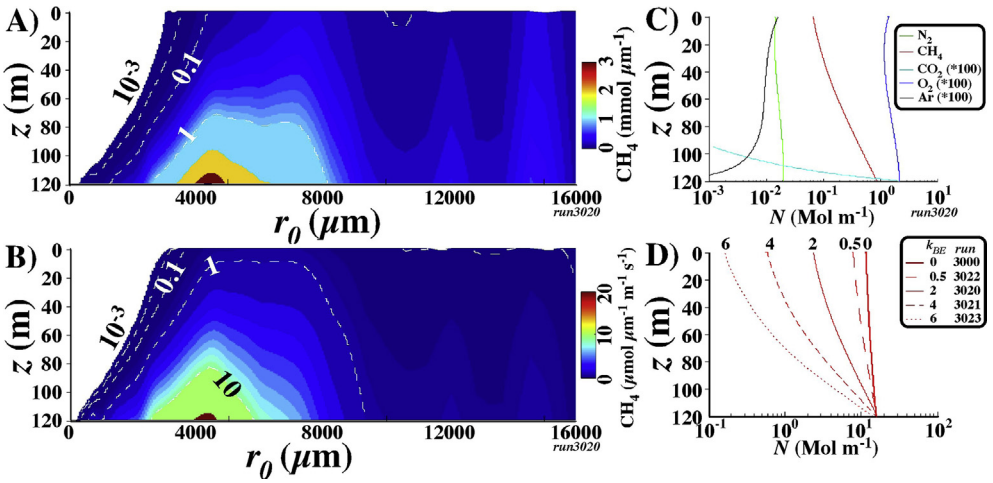

Fig. 15. A) Bubble plume methane, CH_4 molar content at depth, z, and dissolution rate (mass per second per radius unit deposited in a 1-m thick layer) with respect to seabed radius, r_0, and z for global bubble plume Φ, upwelling flow, V_{up} = 100 cm s^{-1}, and enhanced bubble gas exchange, k_{BE} = 2. B) CH_4 dissolution flux. Decadal contours are labeled, 10 color levels per decade. C) Size-integrated z-profile of bubble molar content, N, and D) N_{CH4} for V_{up} = 100 cm s^{-1} and various values of k_{BE}. Data key on figure. *run3000*, *run3020*, *run3021*, *run3022*, *run3023*. (For interpretation of the references to color in this figure legend, the reader is referred to the web version of this article.)

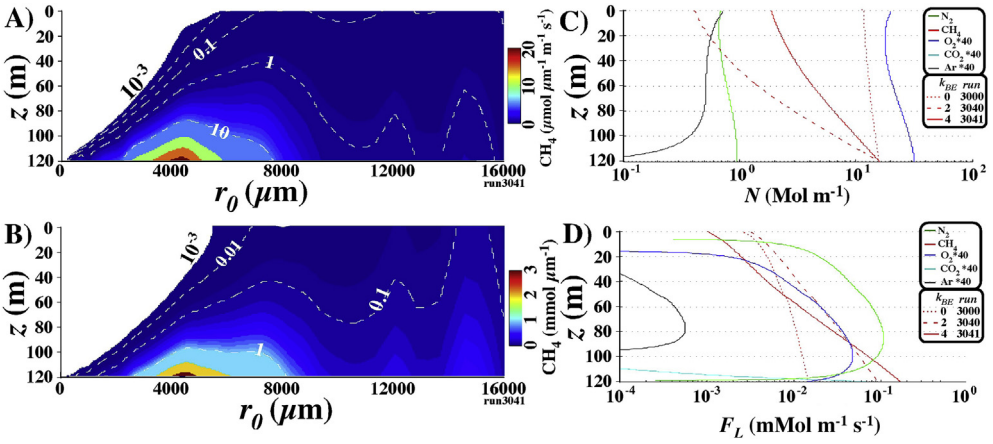

Fig. 16. Simulation output for the global 22/4b bubble plume with enhanced bubble gas exchange, k_{BE} = 2, slow rise k_S = 2, and 100 cm s^{-1} upwelling flow, A) Methane, CH_4, mass content with respect to seabed radius, r_0, and depth, z, and B) CH_4 dissolution flux. Decadal contours are labeled, 10 color levels per decade. C) Size-integrated z-profile of bubble molar content, N, for a same run for all gases, and a range of k_{BE} for CH_4, and D) bubble plume dissolution flux, F_L, for the same range of k_{BE}. Data key on figure. *run3000*, *run3040*, *run3041*. (For interpretation of the references to color in this figure legend, the reader is referred to the web version of this article.)

large bubbles (Leifer, 2015). Seabed bubbles were almost entirely CH_4 (Supp. Table S4) and thus very large bubbles easily should transport significant seabed CH_4 to the upper water-column and atmosphere (Leifer and Patro, 2002) given the moderate water depth (~120 m).

To explore the potential reasons for the observed low impact of the 22/4b megaplume seepage on surface water concentrations and sea-air fluxes, bubble plume simulations were conducted using a synthetic seabed global size distribution (Fig. 7) and observed upwelling flows (Supp. Fig. S5). These simulations showed that for the measured upwelling flows, only quite small bubbles (r_0 < 500 μm) failed to reach the sea surface (Fig. 6) while larger bubbles retain a significant fraction of their seabed CH_4 (Fig. 10). Moreover, video observations clearly showed the presence of numerous large (r_0 > 5000 μm) and very large (r_0 > 10,000 μm) bubbles. Given that very small bubbles (r_0 < 300 μm) appear milky in video (Leifer, 2010) they clearly were unrepresentative of the overall bubble size spectrum in the seabed video survey (Leifer, 2015). Thus, the attempt to produce sufficiently large deep-water column loss rates based on current knowledge of bubble processes, only could constrain CH_4 to the lower water column by assuming unrealistically small bubble sizes that were inconsistent with extensive seabed video data.

Two hypothesized processes were proposed that could have constrained megaplume CH_4 to the deeper water column: Vortical plume motions causing a reduced effective vertical rise rate (Schneider von Deimling et al., 2015) and turbulence-induced enhancement of the individual bubble gas transfer velocity, k_{BE}, proposed in this work. Simple approximations for these hypothesized processes were investigated in numerical simulations and found able to reproduce observations, particularly in combination. Both processes decouple the strict dependency of the gas exchange coefficient on the bubble rise velocity.

5.3. Vortical motions and slow rise

One phenomenon that was observed and proposed to explain in part the constraint of CH_4 to the deeper water-column was the interaction between large vortical structures and rising bubbles. Specifically, bubbles trapped in vortical structures rise slower,

thereby losing additional mass in the deeper water-column. Such distinct turbulence patterns were observed on a range of size scales in video and hydroacoustic data from decimeters to several meters (Schneider von Deimling et al., 2015).

Laminar spiral motions alone would not reduce the bubble "hold-up" time subsurface, because the bubble vertical buoyance force and rise velocity exists independent of laminar lateral displacement. Therefore, we hypothesize that large vortical turbulence motions may have reduced significantly the bubble vertical velocity. Such phenomena have been noted in computation flow studies due to the lift force, which slows bubble rise velocities more strongly with increasing turbulence intensity (Snyder et al., 2007). The phenomenon manifest as a deceleration of the bubble while it is trapped by a vortex, followed by acceleration once the vortex disintegrates (Spelt and Biesheuvel, 1997). The interaction between vortices and bubble rise leads to positive or negative-skew in velocity probability distributions, with the skew dependent on the non-dimensional turbulence intensity. Although Snyder et al. (2007) only calculated this phenomenon for bubbles up to $r \sim 1000$ μm, Grimaldo et al. (2010) observed long-term bubble trapping (minute time-scale) for horizontal roll vortices near the sea surface for larger ($r \sim 2000$ μm) bubbles. Where the vortice's axis has a directional component in the rise direction, vortex-trapping efficiency is reduced and bubble slow rise is less effective.

For illustrative purposes, the slow rise simulations assumed all bubbles were entrained in the vortical fluid motions. In reality, some fraction of bubbles most likely would rise slowly in the vortical fluid flows, while other bubbles would rise normally outside these fluid flow structures. Overall, small vortical tilt (or slow rise) had a significant effect, but for stronger slow rise (greater tilt), sensitivity decreases because the vortices were simulated as entrained and uplifted in the upwelling flow (Fig. 13E).

Although not addressed in this study, to some extent, downwelling flows provide a negative slow rise, which would force dissolution of those bubbles trapped in such flows. Downwelling flows at 22/4b were observed in sonar data (Wilson et al., 2015) and in recirculation flows in the crater (Schneider von Deimling et al., 2015). An interesting possibility related to vortex trapping is that fluid detrainment at the thermocline and subsequent downflows (Schneider von Deimling et al., 2015) also enhances dissolution of trapped bubbles in the deeper water column and returns upwelled CH_4-enhanced fluids back to depth.

5.4. Enhanced individual bubble gas exchange velocity

One proposed process that could explain observations, was that intense bubble megaplumes have enhanced individual bubble gas exchange rates, k_{BE}, compared to the stagnant water parameterizations used in simulations of normal bubble plumes (Clift et al., 1978). For a bubble in stagnant water, k_B is derived from the flow field in the bubble's boundary layer and is generated by the rising bubble's buoyancy. Thus k_B and V_B are intimately linked.

In the case of "enhanced bubble gas exchange rate," we propose that the high bubble concentration in the plume creates and maintains an intense turbulence field with eddies down to size scales comparable to the bubble boundary layer – i.e. 10 μm and smaller. Mechanistically, we propose that in sufficiently dense plumes, this turbulence field is created by the mass of persistent bubble wakes, which form turbulence on bubble size-scales (Shih-Fan et al., 1990). These eddies then add turbulence to the bubble boundary layer, increasing gas transfer, simulated by an additive exchange rate parameterization. This formulation assumes that bubble self-generated turbulence and gas exchange persists for all levels of enhanced bubble gas exchange, with the imposed turbulence field adding to gas exchange.

Simulations showed that even a moderate k_{BE} strongly constrained CH_4 emission to the lower water column (Fig. 15). Importantly, because k_{BE} also enhanced air uptake (Fig. 15C and Supp. Fig. S24), it allowed very large bubbles to reach the sea surface spanning approximately the same size range as at the seabed (Supp. Fig. S25), although smaller bubbles dissolved, particularly for the strongest enhancement ($k_{BE} = 6$, *run3023*). It should be noted that the simulation showed the surfacing bubbles were highly CH_4-depleted. A simulation with $k_{BE} = 6$ (Fig. 15) – where plume turbulence overwhelms bubble-generated turbulence – reduced atmospheric CH_4 fluxes to levels comparable to observations, i.e., two orders of magnitude. Interestingly, the simulations show dissolution dramatically shrinks bubbles by the thermocline before they grow again due to air uptake in the upper water-column. Such small bubbles at the thermocline could be susceptible to detrainment and thus would no longer be in the plume to grow afterwards (as in the simulation).

The k_{BE} formulation is simplistic and was chosen solely to explore the implications to bubble plume fate. In reality, there likely would be a radius dependency in k_{BE}, with enhancement less effective on bubbles smaller than the imposed turbulence size-scales. There also likely is an onset time during the plume's acceleration phase when the turbulence field had not yet become fully developed. Furthermore, if the plume disperses sufficiently, or loses sufficient volume so that the underlying driving Q decreases significantly – such as happened for strong k_{BE} at about the thermocline – turbulence levels will decrease and k_{BE} should approach zero, leading to normal plume behavior. Also, currents are likely to affect k_{BE}, in part by advecting turbulence structures out of the plume (into the downcurrent momentum plume).

Currents can lead to continuous small bubble detrainment, decreasing the volume flux slightly (Leifer et al., 2009) and increasing dissolved plume gas loss to the ambient water column, although dissolved gases were not a significant factor for the 22/4b megaplume. Strong currents can disrupt the bubble plume (Leifer et al., 2015) reducing the upwelling flow. Thus, enhanced bubble dissolution and high currents both increase megaplume CH_4 loss to the water column. However, data show strong upwelling flows persisting across most of the water column (Supp. Fig. S5), thus current disruption was insufficient to reduce the buoyancy driving the upwelling flow.

Stratification disrupts upwelling flows by requiring more work by the plume against a stronger density gradient, leading to enhanced plume detrainment and momentum loss (Asaeda and Imberger, 1993). A vertical profile of V_{up} in the upper water column for Trilogy Seep in the Coal Oil Point seep field demonstrated a flow regime where stratification decreased V_{up} in the upper water column (Leifer et al., 2009). Lower currents and the wave mixed layer's shallowness (10 or so meters) in the Coal Oil Point seep field, may explain why Trilogy Seep surface bubbles (45 m depth) have an air content consistent with minimal CH_4 loss to the water column (Clark et al., 2010), in strong contrast to the fate of bubbles at the 22/4b site.

5.5. Enhanced bubble transfer hypothesis

The effect of enhanced bubble transfer is to cause CH_4 and other gases to outflow the bubble far faster than normal and for faster gas uptake than normal. Currently, although the model simulations show it is consistent with observations and can explain them, in contrast to any other known mechanism, this does not validate the mechanism. Given its potential importance to processes such as the fate of anthropogenic and natural blowouts, validation clearly is merited. Simulations herein incorporated both major gases (O_2, N_2, CH_4) and trace gases (CO_2 and Ar).

The fate of each of the different gases is different in each bub-

ble, thus data on the changing bubble composition, or for seep gases, dissolution fluxes, provide a powerful modeling constraint, if coupled with bubble size distribution measurements. Thus, hypothesis validation – in the field or laboratory – should combine *in situ* multi-component measurements at different heights above the seabed/source with bubble size distribution measurements, focusing on the ratio between different gases for dissolved gas measurements. Water-column measurements always have some uncertainty due to dissolved plume transport; however, plume transport does not discriminate between gases, unlike bubble-mediated transport.

5.6. Broader implications

To date, these data are the most complete ever collected at a blowout megaplume – including Deepwater Horizon (Leifer, personal observation, 2013) – and suggest unique megaplume processes that affect our understanding of the fate of the CH_4 in these large bubble plumes. Megaplumes may occur due to anthropogenic accidents, such as at the 22/4b site, or by natural processes where shallow gas breaches to the seabed, such as occurred for the Seep Tent Seep in the Coal Oil Point seep field (Boles et al., 2001). The enhanced gas exchange megaplume hypothesis clearly requires validation. If confirmed, this would suggest that in terms of atmospheric budgets from natural marine seepage, the role of *non-megaplume* bubble plume gas transfer should be emphasized on a global basis (Leifer and Patro, 2002). Data presented herein from the 22/4b site show that the upscaling of current bubble plume knowledge based on observations from strong seepage locations, characterized by enhanced vertical CH_4 transport due to stronger upwelling flows, is inappropriate for megaplumes, presumably due to unique fluid dynamic processes.

6. Conclusions

Data from air and water column surveys of the 22/4b site indicate that under conditions of strong stratification common in summer and fall, the megaplume transfers a very small fraction of seabed CH_4 to the upper water column or to the atmosphere, on the order of 1% or less. This was unexpected, particularly because of the observed very strong, upwelling flows, which should allow all but the smallest bubbles to reach the sea surface with significant CH_4 concentrations. A numerical bubble propagation model was used to better understand the underlying mechanisms of this disagreement between observations and theory. The model was initialized with a bubble plume size distribution synthesized from literature bubble plume size distributions and the video survey plume class probability distributions. Investigation of the different plume class types identified in the video surveys indicated that all plume classes observed contained sufficiently large bubbles that should transport far more CH_4 to the sea surface than suggested by observations.

To reconcile observations with model predictions, two new, hypothesized megaplume fluid dynamic processes were simulated: megaplume-enhanced individual bubble gas exchange rate and slow bubble vertical rise due to large vortical motions, the later revealed in hydroacoustic data. For enhanced bubble gas exchange, plume turbulence is hypothesized to affect the bubble boundary layer. Numerical simulations showed that this could explain observations. Slowed vertical rise also could have played a role but was unable to explain observations on its own.

If validated, these processes have significant implications for understanding the fate of CH_4 from megaplume emissions (anthropogenic or natural) and suggests focusing attention on smaller and more dispersed bubble plumes with respect to assessing contribution of natural marine seepage to greenhouse gas budgets.

Acknowledgment

We would like to thank the crew of the Noordhoek Pathfinder, for help with data collection, as well as Simon Dewing, ExxonMobil, for data collection, and Joe Smith, Simon Dewing, and Gary Robertson, ExxonMobil for data and report quality review.

Appendix A. Supplementary data

Supplementary data related to this article can be found at http://dx.doi.org/10.1016/j.marpetgeo.2015.07.025.

References

Asaeda, T., Imberger, J., 1993. Structure of bubble plumes in linearly stratified environments. J. Fluid Mech. 249, 35–57.
Boles, J.R., Clark, J.F., Leifer, I., Washburn, L., 2001. Temporal variation in natural methane seep rate due to tides, coal oil point area, California. J. Geophys. Res. Oceans 106, 27077–27086.
Clark, J.F., Washburn, L., Schwager, K., 2010. Variability of gas composition and flux intensity in natural marine hydrocarbon seeps. Geo Mar. Lett. 30, 379–388.
Clift, R., Grace, J.R., Weber, M.E., 1978. Bubbles, Drops, and Particles. Academic Press, New York.
Coffin, R.B., Smith, J.P., Plummer, R.E., Yoza, B., Larsen, R.K., Millholland, L.C., Montgomery, M.T., 2013. Spatial variation in shallow sediment methane sources and cycling on the Alaskan Beaufort Sea Shelf/Slope. Mar. Petrol. Geol. 45, 186–197.
Deane, G.B., Stokes, M.D., 2002. Scale dependence of bubble creation mechanisms in breaking waves. Nature 418, 839–844.
Gerilowski, K., Krings, T., Buchwitz, M., Hartmann, J., Sachs, T., Erzinger, J., Burrows, J.P., Bovensmann, H., 2015. Methane remote sensing constraints on direct sea-air flux from the 22/4b North Sea massive blowout bubble plume. J. Mar. Petrol. Geol. (in this issue).
Grimaldo, E., Leifer, I., Gjøsund, S.H., Larsen, R.B., Jeuthe, H., Basedow, S., 2010. Field demonstration of a novel towed, area bubble-plume zooplankton (Calanus sp.) harvester. Fish. Res. 107, 147–158.
Judd, A., 2015. Methane emissions from the 22/4b blow-out site in the context of the North Sea. J. Mar. Petrol. Geol. (in this issue).
Kvenvolden, K.A., Rogers, B.W., 2005. Gaia's breath-global methane exhalations. Mar. Petrol. Geol. 22, 579–590.
Leifer, I., 1995. A Validation Study of Bubble Mediated Air-sea Gas Transfer Modeling, Earth and Atmospheric Sciences (Ph.D. thesis). Georgia Institute of Technology, Atlanta, p. 205.
Leifer, I., 2010. Characteristics and scaling of bubble plumes from marine hydrocarbon seepage in the coal oil point seep field. J. Geophys. Res. 115, C11014.
Leifer, I., 2015. Seabed bubble flux estimation by calibrated video survey for a large blowout seep in the North Sea. J. Mar. Petrol. Geol. (in this Issue).
Leifer, I., Boles, J.R., Luyendyk, B.P., Clark, J.F., 2004. Transient discharges from marine hydrocarbon seeps: spatial and temporal variability. Environ. Geol. 46, 1038–1052.
Leifer, I., Clark, J.F., 2002. Modeling trace gases in hydrocarbon seep bubbles: application to marine hydrocarbon seeps in the Santa Barbara Channel. Russ. J. Geol. Geophys. 47, 572–579.
Leifer, I., Clark, J.F., Chen, R.F., 2000a. Modifications of the local environment by natural marine hydrocarbon seeps. Geophys. Res. Lett. 27, 3711–3714.
Leifer, I., Culling, D., 2010. Formation of seep bubble plumes in the coal oil point seep field. Geo Mar. Lett. 30, 339–353.
Leifer, I., Jeuthe, H., Gjøsund, S.H., Johansen, V., 2009. Engineered and natural marine seep, bubble-driven buoyancy flows. J. Phys. Oceanogr. 39, 3071–3090.
Leifer, I., Judd, A., 2015. The UK22/4b blowout 20 years on: investigations of continuing methane emissions from sub-seabed to the atmosphere in a North Sea context. J. Mar. Petrol. Geol. (in this Issue).
Leifer, I., Kamerling, M., Luyendyk, B.P., Wilson, D., 2010. Geologic control of natural marine hydrocarbon seep emissions, coal oil point seep field, California. Geo Mar. Lett. 30, 331–338.
Leifer, I., Luyendyk, B.P., Boles, J., Clark, J.F., 2006. Natural marine seepage blowout: contribution to atmospheric methane. Glob. Biogeochem. Cycles 20.
Leifer, I., McClimans, T.A., Gjøsund, S.H., Grimaldo, E., 2015. Fluid motions associated with engineered area bubble plumes. J. Waterw. Port Coast. Ocean Eng. http://dx.doi.org/10.1061/(ASCE)WW.1943-5460.0000292, (in press).
Leifer, I., Patro, R.K., 2002. The bubble mechanism for methane transport from the shallow sea bed to the surface: a review and sensitivity study. Cont. Shelf Res. 22, 2409–2428.
Leifer, I., Patro, R.K., Bower, P., 2000b. A study on the temperature variation of rise velocity for large clean bubbles. J. Atmos. Ocean. Technol. 17, 1392–1402.
Lemckert, C.J., Imberger, J., 1993. Energetic bubble plumes in arbitrary stratification. J. Hydraul. Eng. 19, 680–703.
Matsunagi, G., Miyanaga, Y., 1990. A field study on the characteristics of air bubble plume in a reservoir. J. Hydrosci. Hydraul. Eng. 8, 65–77.
McGinnis, D.F., Greinert, J., Artemov, Y., Beaubien, S.E., Wüest, A., 2006. Fate of rising methane bubbles in stratified waters: how much methane reaches the atmosphere? J. Geophys. Res. 111 C09007.

Nauw, J., de Haas, H., Leifer, I., Rehder, G., 2015a. A review of oceanographic and meteorologic controls on the fate of North Sea methane from a seabed source. J. Mar. Petrol. Geol. (in this issue).
Nauw, J., Linke, P., Leifer, I., 2015b. A note on bubble plumes and orographic forcing: mechanisms of autumn North Sea stratification breakdown. J. Mar. Petrol. Geol. (in this issue).
NOAA, 2013. Ocean Station M http://www.esrl.noaa.gov/gmd/dv/data/?site=STM.
Otto, L., Zimmerman, J.T.F., Furnes, G.K., Mork, M., Saetre, R., Becker, G., 1990. Review of the physical oceanography of the North Sea. Neth. J. Sea Res. 26, 161–238.
Patro, R., Leifer, I., Bowyer, P., 2002. Better bubble process modeling: improved bubble hydrodynamics parameterisation. In: Donelan, M., Drennan, W., Salzman, E.S., Wanninkhof, R. (Eds.), Gas Transfer and Water Surfaces. American Geophysical Union, Washington, pp. 315–320.
Ravelet, F., Colin, C., Risso, F., 2011. On the dynamics and breakup of a bubble rising in a turbulent flow. Phys. Fluids 23, 103301.
Reeburgh, W.S., 2007. Oceanic methane biogeochemistry. Chem. Rev. 107, 486–513.
Rehder, G., Keir, R.S., Suess, E., Thomas, P., 1998. The multiple sources and patterns of methane in North Sea waters. Aquat. Geochem. 4, 403–427.
Rehder, G., Leifer, I., Brewer, P.G., Friederich, G., Peltzer, E.T., 2009. Controls on methane bubble dissolution inside and outside the hydrate stability field from open ocean field experiments and numerical modeling. Mar. Chem. 114, 19–30.
Schneider von Deimling, J., Brockhoff, J., Greinert, J., 2007. Flare imaging with multibeam systems: data processing for bubble detection at seeps. Geochem. Geophys. Geosys. 8, 1–7.
Schneider von Deimling, J., Rehder, G., Linke, P., Judd, A., 2015. Ongoing methane discharge at well site 22/4b (North Sea) and discovery of spiral vortex bubble plume motions. J. Mar. Petrol. Geol. (in this issue).
Shakhova, N., Semiletov Igor, P., Leifer, I., Sergienko, V., Salyuk, A., Kosmach, D., Chernikh, D., Stubbs, C., Nicolsky, D., Tumskoy, V., Alexeev, V., Gustafsson, O., 2014. Ebullition and storm-induced methane release from the East Siberian Arctic shelf. Nat. Geosci. 7, 64–70.
Shih-Fan, L., Tsuchiya, K., Brenner, H., 1990. Bubble Wake Dynamics in Liquids and Liquid-solid Suspensions. Butterworth-Heinemann, Stoneham, MA.
Snyder, M.R., Knio, O.M., Katz, J., Le Maître, O.P., 2007. Statistical analysis of small bubble dynamics in isotropic turbulence. Phys. Fluids 19, 065108.
Socolofsky, S.A., Adams, E.E., Sherwood, C.R., 2011. Formation dynamics of subsurface hydrocarbon intrusions following the deepwater horizon blowout. Geophys. Res. Lett. 38, L09602.
Solomon, E., Kastner, M., MacDonald, I.R., Leifer, I., 2009. Considerable methane fluxes to the atmosphere from hydrocarbon seeps in the Gulf of Mexico. Nat. Geosci. 2, 561–565.
Spelt, P.D.M., Biesheuvel, A., 1997. On the motion of gas bubbles in homogeneous isotropic turbulence. J. Fluid Mech. 336, 221–244.
Watanabe, S., Tsurushima, N., Kusakabe, M., Tsunogai, S., 1995. Methane in Izena Cauldron, Okinawa Trough. J. Oceanogr. 51, 239–255.
Wiesenburg, D.A., Guinasso, N.L., 1979. Equilibrium solubilities of methane, carbon monoxide, and hydrogen in water and sea water. J. Chem. Eng. Data 24, 356–360.
Wiggins, S., Hildebrand, J., Leifer, I., 2015. Long-term acoustic monitoring at North Sea well site 22/4b. J. Mar. Petrol. Geol. (in this issue).
wikipedia commons, 2015. North Sea Map. wikipedia.
Wilson, D., Leifer, I., Maillard, E., 2015. Megaplume bubble process visualization by 3D multibeam sonar mapping. J. Mar. Petrol. Geol. (in this Issues).

Glossary

b: power law coefficient in equation $V_{up} \sim Q^b$ (−)
C: aqueous concentration (mol/cm^3)
C_1: methane concentration (molar)
C_2: ethane concentration (molar)
C_3: propane concentration (molar)
C_4: butane concentration (molar)
dN_i/dz : plume molar dissolution rate for gas i (mol/m/s)
f: bubble mass flux (mol/s)
F_L: layer dissolution rate (plume dissolution flux) distribution (mol/m/s)
g: gravitational constant (cm/s^2)
H: Henry's Law constant (mol/cm^3 / atm)
i: gas index (−)
j: plume class (−)
k_B: individual bubble gas exchange velocity (cm/s)
k_{BE}: enhanced individual bubble gas exchange rate (−)
k_{BN}: new individual bubble gas exchange rate (cm/s)
k_β: depth solubility correction from Henry's Law (−)
k_S: slow rise factor (−)
M_j: number of plumes in bubble plume class j (#)
n: total bubble molar content (mol)
n_i: bubble molar content of gas i (mol)
N_i: plume molar content of gas i (mol)
N_{SS}: plume moles at sea surface (flux to atmosphere) (mol/s)
P_A: atmospheric pressure (atm)
P_B: bubble pressure (atm)
P_i: bubble partial pressure of gas i (atm)
Q: volume flux (L/s)
R: ideal gas constant (atm cm^3 / Mol °C)
R_{sample}: sample isotope ratio (‰)
$R_{standard}$: standard isotope ratio (‰)
r: bubble equivalent spherical radius (μm)
r_o: bubble radius at seabed (μm)
r_f: bubble radius at sea surface (μm)
$R_{Standard}$: $^{13}C/^{12}C$ the reference standard (−)
Sc: Schmidt number (−)
S_F: scaling factor from individual plume Q to global plume Q (−)
T: temperature (°C)
t: time (s)
V_B: bubble stagnant fluid rise velocity (cm/s)
V_F: fluid velocity (including V_{up}) (cm/s)
V_{up}: fluid upwelling velocity driven by bubble plume (cm/s)
X: number of data points (−)
z: depth coordinate (cm)
z_o: seabed depth (cm)
z_d: dissolution depth (cm)
Γ: percent of seabed molar flux transported to sea surface (%)
$\delta^{13}C$: carbon 13 isotope fraction (‰)
ζ: compressibility (-)
ρ_w: water density (g/cm^3)
σ: surface tension (LaPlace pressure) (atm-cm)
ϕ: bubble plume size distribution (#/μm/cm^3)
Φ: global bubble size distribution (summed over vents) (#/μm/cm^3)